Vrije Universiteit Brussel

VRIJE
UNIVERSITEIT
BRUSSEL

Remote sensing estimation of urban surface evapotranspiration based on a modified Penman–Monteith model

Zhang, Yu; Li, Long; Qin, Kai; Wang, Yuchen; Chen, Longqian; Yang, Xiaoyan

Remote sensing estimation of urban surface evapotranspiration based on a modified Penman–Monteith model

Yu Zhang
Long Li
Kai Qin
Yuchen Wang
Longqian Chen
Xiaoyan Yang

SPIE.

Remote sensing estimation of urban surface evapotranspiration based on a modified Penman–Monteith model

Yu Zhang,[a,b] Long Li,[a,c] Kai Qin,[a] Yuchen Wang,[a] Longqian Chen,[a,*] and Xiaoyan Yang[a,b]

[a]China University of Mining and Technology, School of Environmental Science and Spatial Informatics, Xuzhou, China

[b]Jiangsu Normal University, School of Geography, Geomatics and Planning, Xuzhou, China

[c]Vrije Universiteit Brussel, Department of Geography, Earth System Science, Brussels, Belgium

Abstract. To date, remote sensing-based algorithms for inferring urban surface evapotranspiration (ET) remain little studied. Based on the modifications of the remote sensing Penman–Monteith (RS-PM) model, we propose an urban RS-PM model for estimating urban surface ET. Compared with the traditional RS-PM model, our urban RS-PM model is specifically developed for urban areas and is characterized by the following improvements: (1) excluding the interference of impervious surface components in urban areas by replacing the vegetation cover fraction index with land surface component fraction parameters inversed through linear spectral mixture analysis for calculating the area proportions of vegetation and soil; (2) considering the effect of the component fractions of vegetation or soil on all energy components of the surface energy balance by applying the modified multisource parallel model for estimating the component latent heat flux; and (3) optimizing the calculation of the component net radiation flux by considering the component surface characteristics. This urban RS-PM model was tested on an urban area of Xuzhou in the eastern Chinese province of Jiangsu. Landsat 8 operational land imager and thermal infrared sensor satellite images acquired between 2014 and 2016, together with their corresponding meteorological data and flux observation data, were used for estimating the ET of the study area for eight dates with the model. The results were validated by the latent heat flux data observed by an open path eddy covariance system. Validation shows the goodness of fit (R^2), the root-mean-square error, the mean relative error, and the correlation coefficient (r) between estimated ET and observed ET for the eight dates were 0.8965, 24.14 W · m^{-2}, 18.5%, and 0.9546, respectively. The results prove that the urban RS-PM model is effective in estimating ET of urban areas with an acceptable accuracy. © *2018 Society of Photo-Optical Instrumentation Engineers (SPIE)* [DOI: 10.1117/1.JRS.12.046006]

1 Introduction

Evapotranspiration (ET) is the sum of the water evaporation and vegetation transpiration, which plays an important role in regulating global energy and water distribution. Traditional ET observation methods, such as porometer,[1,2] lysimeter,[3] water balance,[4–7] Bowen ration,[8,9] Scintillometer,[10,11] and sap-flow,[12–15] or estimation methods such as the Penman–Monteith (P-M)[16–18] model, are mostly applied on a point, field, or basin scale with high ET estimation accuracy. However, these methods are inapplicable to large-scale ET estimation. Recent remote sensing advances have enabled regional ET estimation from satellite image data. At present,

the available ET estimation methods are generally applied to natural or agricultural surfaces,[19] but few have been developed specifically for urban areas. Urban areas are important carriers of human living and productive activities, which have a significant impact on the regional climate change and energy exchange. As a key link in the regional water cycle and surface energy balance (SEB), ET has a regulating effect on regional climate and heat environment in urban areas which cannot be ignored. Therefore, it is necessary to develop an applicable algorithm for estimating the land surface ET of urban areas.

The most widely used remote sensing-based ET estimation methods include the SEB models[20,21] and the remote sensing Penman–Monteith (RS-PM) models.[22,23] The SEB models can be broadly divided into the one-source and the dual-source. The one-source SEB models such as surface energy balance index,[24–26] surface energy balance algorithm for land (SEBAL),[20,21,27] simplified surface energy balance index (S-SEBI),[28–30] and surface energy balance system,[31–34] do not distinguish between vegetation and soil; they consider a regional surface, regardless of the spatial structure of the surface, as one big leaf—momentum, heat, and water vapor are exchanged with the outside space through this large "leaf." Such SEB models are appropriate for homogeneous and closed vegetation areas, rather than for urban areas with varied land cover types. The dual-source models are either serial or parallel, depending on how the coupling between canopy and soil is considered.[35–37] The parallel models assume that the canopy and soil exchange both water vapor and heat with the atmosphere independently, and the transmissions through canopy and soil are parallel without a coupling effect on each other. Zheng[38] proposed a multisource parallel model for estimating urban ET based on the dual-source parallel model by adding the impervious surface component in the SEB equation. Based on Zheng's model, Zhang et al.[39] then developed the multisource parallel model with optimized calculations of the component net radiation and the component fractions of vegetation and soil. However, the multisource parallel model[39] relies heavily on remote sensing data with multiple thermal infrared bands to calculate the component temperatures of vegetation and soil, which is a key parameter in the model.[32] Remote sensing data with multiple thermal infrared bands, such as those acquired by advanced spaceborne thermal emission and reflection radiometer (ASTER) and moderate-resolution imaging spectroradiometer (MODIS) sensors, have limited applications, because ASTER's short-wave infrared (SWIR) detectors have failed since 2008[40] and the low spatial resolution (1 km) of MODIS data is not quite suitable for urban scale studies.[39]

The Penman–Monteith (P-M) model has been widely used, as its parameters can be calculated through conventional meteorological data.[16] Cleugh et al.[22] were first to propose an integration between remote sensing data and the P–M model. The first remote sensing P–M (RS-PM) model used a simple algorithm to estimate the canopy conductance but did not take soil evaporation into consideration.[41] Mu et al.[23] developed a new RS-PM model, which has improved the conductance calculation and estimated soil evaporation by introducing the complementary relationship hypothesis into the P–M model.[41] Mu et al.[42] further developed their RS-PM model by distinguishing daily and nightly ET. Yuan et al.[43] revised the model proposed by Mu et al.[42] by including the effect of air temperature on stomatal conductance and by replacing the enhanced vegetation index (EVI) with the leaf area index (LAI) for calculating the vegetation coverage fraction. Zhang et al.[44,45] proposed an RS-PM model based on NDVI called the process-based land surface ET /heat fluxes algorithm, which they used to estimate the global ET for the 1983–2006 period. In addition, Leuning et al.[46] developed their own model called the Penman–Monteith Leuning model and reported accurate global and regional ET estimations. Despite their wide applications to natural or agricultural surfaces, these RS-PM models are still unsuitable for urban areas, which are characterized by spectral heterogeneous land covers. To increase the applicability of the RS-PM model, we propose in this study a modified RS-PM model called the urban RS-PM model based on Mu et al.'s RS-PM model[23] and the multisource parallel model.[39] By combing the vegetation and soil fractions extracted through linear spectral mixture analysis (LSMA, aka linear spectral unmixing) of satellite images over urban areas, the vegetation transpiration and the soil evaporation in urban areas can be estimated separately. The urban ET provides key information for urban heat island regulation mechanism studies and the improvement of urban environment.

2 Study Area and Data

2.1 Study Area

The built-up area of Xuzhou in the eastern Chinese province of Jiangsu (Fig. 1) has been selected as the study area to test the proposed urban RS-PM model. Xuzhou (33°43′ to 34°58′N, 116°22′ to 118°40′E) is the second-largest city of Jiangsu province and covers a geographical area of 3037 km². Located at the junction of the provinces of Jiangsu, Shandong, Henan, and Anhui, Xuzhou is known as an important comprehensive transportation and logistics hub in China. Xuzhou is generally flat and is characterized by low elevations ranging from 30 to 50 m. Affected by the monsoon climate of medium latitudes, Xuzhou has heavy precipitation and insolation, with an average annual temperature of 15.5°C, an average annual rainfall of 800 to 930 mm, an average annual sunshine period of 2284 to 2495 h, and an average annual frost-free period of 200 to 220 days. In addition, the forest coverage rate is 30.3% and the ratio of built-up area to the total area has reached 43.3%. By the end of 2016, the urban population of Xuzhou reached 8.71 million, with an urbanization rate of 62.44%, indicating that Xuzhou has become a highly urbanized city. These features have enabled the built-up area of Xuzhou to become an ideal area for estimating urban ET with our urban RS-PM model.

2.2 Data

2.2.1 Remote sensing data

To extract the information of urban surface component fractions and temperatures, remote sensing images with multispectral and thermal infrared bands are required. Landsat 8 satellite carries an operational land Imager (OLI) and a thermal infrared sensor (TIRS):[47] the OLI includes nine bands at 30-m spatial resolution except for the panchromatic band (15 m); the TIRS produces two thermal infrared bands at 100-m spatial resolution. In this study, the first seven multispectral bands were used to extract endmember fractions of the study area, and the TIRS band B10 was used to obtain the land surface temperature. As our available flux data, used for validation (detailed in Sec. 2.2.2), were observed between 2014 and 2016, and the observation was not continuous during the period, we selected eight Landsat 8 images of the study area from 2014 to 2016 (Table 1).

To assess the accuracy of component fractions estimated from the Landsat 8 data, high-resolution remote sensing data are also required. Data from Chinese Earth observation satellites Gaofen-1 (GF-1) and Gaofen-2 (GF-2) can be a good choice as their panchromatic bands are
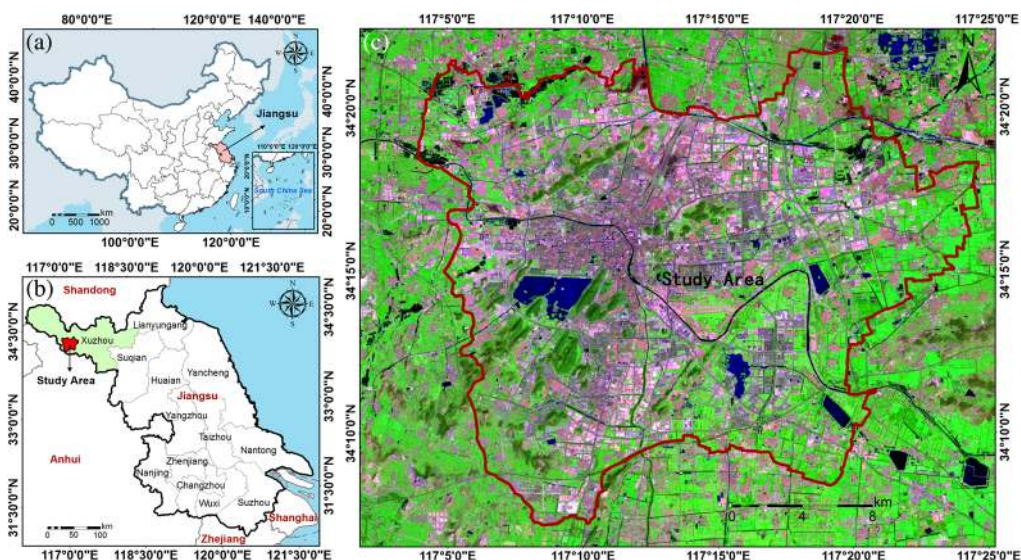

Fig. 1 The built-up area of Xuzhou was selected as the study area: (a) Jiangsu province in China, (b) Xuzhou in Jiangsu province, and (c) the study area extracted and shown on a false color Landsat 8 image (September 04, 2016, $R:G:B =$ b7:b5:b3).

Table 1 Landsat 8 images used in this study.

No.	Scene ID	Acquisition date	Acquisition time (GMT)
1	LC81210362014121LGN00	May 01, 2014	02:42:29
2	LC81210362014297LGN00	September 24, 2014	02:42:58
3	LC81220362015355LGN00	December 21, 2015	02:49:04
4	LC81210362016047LGN01	February 14, 2016	02:42:40
5	LC81220362016070LGN01	March 10, 2016	02:48:47
6	LC81220362016246LGN00	September 02, 2016	02:49:07
7	LC81220362016278LGN00	October 04, 2016	02:49:11
8	LC81220362016310LGN00	November 05, 2016	02:49:16

Table 2 GF-1 or GF-2 images used for LSMA validation. Note that the two September 24, 2014 scenes were merged for covering the entire study area and that Beijing time = GMT + 8.

Satellite	No.	Scene ID	Acquisition Date	Acquisition Time (Beijing)
GF-1	1	579,791	September 24, 2014	11:26:39
	2	579,790	September 24, 2014	11:26:34
	3	2,979,014	November 04, 2016	11:36:44
GF-2	4	2,872,975	September 05, 2016	11:25:48

acquired at 2- and 1-m resolution, respectively, both sufficient for LSMA validation. Based on the acquisition dates of the Landsat 8 data, four Gaofen images were selected (Table 2).

2.2.2 Flux data

Latent heat flux data were also collected to assess the accuracy of the study area's ET estimated by the urban RS-PM model. The flux data were observed with an open path eddy covariance (EC) system, which was set up on a flux tower at the Collaborative Observation Testing Site affiliated to China University of Mining and Technology (CUMT-COTS) (Fig. 2). The aerodynamic parameters about the setup and its surroundings are shown in Table 3. The missing data and abnormal data due to instrument malfunction, poor maintenance, and bad weather conditions were gap-filled by the mean diurnal variations method.[48,49]

2.2.3 Meteorological data

Meteorological data for calculating parameters required for the urban RS-PM model were also obtained at almost the same time as the Landsat image data were acquired from at the CUMT-COTS. The parameters include air temperature (T_{air}), relative humidity (RH), wind speed (u_z), and atmospheric pressure (P_A) measured at the height of 2 m (Table 4).

3 Methodology

3.1 Urban Remote Sensing Penman–Monteith Model

In this section, we will introduce the framing of the urban PS-PM model and highlight its improvements over the traditional RS-PM model in Secs. 3.1.2–3.1.4.
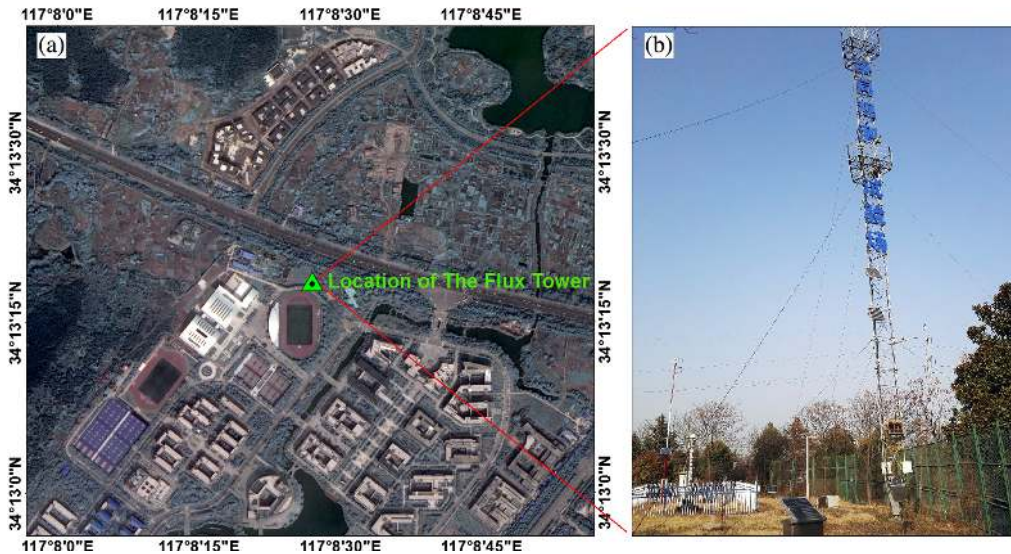
Fig. 2 The flux tower at the Collaborative Observation Testing Site affiliated to China University of Mining and Technology: (a) location and (b) photograph.

Table 3 Aerodynamic parameters around the flux tower.

Aerodynamic parameters	Physical meaning	Measurements (m)
Z	EC height from ground	15
h_b	Average building height	4.5
d	Zero displacement	0.68
Z_{om}	Momentum roughness length	3
$Z - d$	Effective measurement of height	14.32

Table 4 Basic meteorological data of study area.

Date	Parameter			
	T_{air} (K)	RH (%)	u_z (m/s)	P_A (kPa)
May 01, 2014	297.42	55.12	2.66	101.12
October 24, 2014	293.59	65.59	2.51	101.62
December 21, 2015	277.96	51.75	1.03	102.69
February 16, 2016	276.50	33.87	2.47	102.54
March 10, 2016	278.34	24.63	1.79	103.19
September 02, 2016	303.92	32.16	2.54	100.24
September 04, 2016	296.25	67.94	2.65	101.42
November 05, 2016	291.38	65.43	1.67	101.08

3.1.1 Algorithm of the traditional remote sensing Penman–Monteith model

The traditional RS-PM model proposed by Mu et al.[23] can be expressed as the sum of vegetation transpiration and soil evaporation:

$$\text{LE} = \lambda E = \lambda E_v + \lambda E_s, \tag{1}$$

where LE refers to latent heat flux that can be expressed as a product of ET and latent heat of vaporization λ; and λE, λE_v, and λE_s, which refer to the total latent heat flux, the latent heat flux of vegetation transpiration, and the latent heat flux of soil evaporation, respectively. It is necessary to determine the fractions of vegetation and soil in a mixed pixel before calculating ET. In the model by Mu et al.,[23] the proportions of vegetation and soil in each remote sensing image pixel are estimated by the vegetation coverage fraction, given as

$$F_C = \frac{\text{EVI} - \text{EVI}_{\min}}{\text{EVI}_{\max} - \text{EVI}_{\min}}, \tag{2}$$

where F_C refers to the vegetation coverage fraction calculated through the EVI.

For vegetation transpiration, λE_v can be estimated as

$$\lambda E_v = \frac{\Delta A_c + \rho C_p \text{VPD}/r_{ah}}{\Delta + \gamma \left(1 + \frac{r_{s,v}}{r_{ah}}\right)}, \tag{3}$$

where Δ is the slope of the curve relating saturated water vapor pressure to temperature, A_c, to the available energy of vegetation ($\text{W} \cdot \text{m}^{-2}$) with $A_c = R_n F_C$; R_n is the net radiation ($\text{W} \cdot \text{m}^{-2}$), G is the soil heat flux ($\text{W} \cdot \text{m}^{-2}$), ρ is the air density ($\text{kg} \cdot \text{m}^{-3}$), C_p refers to the air specific heat capacity ($\text{J} \cdot \text{kg}^{-1} \cdot \text{K}^{-1}$), VPD is the difference between saturated vapor pressure (e_s) and the actual water vapor pressure (e_a), in unit of Pa, i.e., $\text{VPD} = e_s - e_a$ (Pa), r_{ah} is the aerodynamic resistance to heat transfer (s·m^{-1}), γ is the psychrometric constant ($\text{Pa} \cdot \text{K}^{-1}$), and $r_{s,v}$ is the canopy surface resistance (s·m^{-1}), respectively.

For soil evaporation λE_s, Mu et al.[23] took potential soil evaporation and the interaction between surface and atmosphere (expressed by vapor pressure deficit and relative humidity) into consideration and proposed an algorithm for it:

$$\lambda E_s = \left(\frac{\text{RH}}{100}\right)^{\text{VPD}/100} \times \frac{\Delta A_{\text{soil}} + \rho C_p \text{VPD}/r_{ah}}{\Delta + \gamma \left(1 + \frac{r_{\text{tot}}}{r_{ah}}\right)}, \tag{4}$$

where RH is the relative humidity (%), A_{soil} is the available energy of soil ($\text{W} \cdot \text{m}^{-2}$) with $A_{\text{soil}} = R_n(1 - F_C) - G$. Here, and r_{tot} is the total aerodynamic resistance to vapor transport (s·m^{-1}),[50] which can be estimated through correcting the total aerodynamic resistance under standard conditions for air temperature and pressure:

$$r_{\text{corr}} = \frac{1.0}{\left(\frac{273.15+T}{293.15}\right)^{1.75} \times \frac{101.3}{P_A}}, \tag{5}$$

$$r_{\text{totc}} = 107.0, \tag{6}$$

$$r_{s,s} = r_{\text{totc}} \times r_{\text{corr}}, \tag{7}$$

where r_{corr} is the corrected total aerodynamic resistance; r_{totc} is a constant (107 s·m^{-1}).[51] Note that T and P_A refer, respectively, to air temperature and pressure under standard conditions with $T = 20°C$ and $P_A = 101.3$ kPa, respectively.

Mu et al.[23] innovated the RS-PM model by including soil evaporation and thus enhanced its applicability. However, there are two major problems when applying the RS-PM model by Mu et al.[23] (henceforth referred to as the traditional RS-PM model) to urban areas with complex underlying surfaces. First, the traditional RS-PM model is mainly applied to natural or agricultural surfaces, which assumes that the land surface is simply covered by vegetation and soil. Therefore, the traditional RS-PM model has used the vegetation coverage fraction F_C and $(1 - F_C)$ to calculate the proportions of vegetation and soil in mixed pixels of remote sensing images. This is not the case for urban areas, because the impervious surface is

a major component that dominates their varied land cover types,[52] and medium-resolution remote sensing image pixels of urban areas are very likely to be mixing pixels that contain an impervious surface component. Second, in the calculation of the available energies (A_c and A_{soil}), the traditional RS-PM model only calculates the component net radiation based on the component fractions of vegetation and soil, without considering the effect of the component fraction variation on other component energies. In addition, the traditional RS-PM model directly uses a pixel's mean net radiation to calculate the component available energies of vegetation and soil. However, component net radiation should be calculated separately due to the spectral heterogeneity between vegetation components and soil components, which has a significant impact on the surface net radiation.

To be able to apply the RS-PM model to urban areas, the urban RS-PM model combines linear spectral mixture analysis and a modified multisource parallel model proposed by Zhang et al.,[39] which can estimate vegetation transpiration and soil evaporation in a spectrally heterogeneous urban context.

3.1.2 *Improving the calculation of vegetation and soil proportions*

Ridd[53] has proposed the V-I-S model to calculate land surface component fractions in mixing pixels of satellite images over urban areas, which divides the land surface components into vegetation, soil, and impervious surface. Small[54] further classified the impervious surface component into two types: high-albedo and low-albedo impervious surfaces (henceforth referred to as high- and low-albedo, respectively). The concepts of high- and low-albedo impervious surface were also adopted by Wu et al.[55] in their LSMA for an urban area. It is noted that in many of the previous studies that have focused on the extraction of component fractions in urban surfaces,[56–58] urban shadow (e.g., building shadow and tree shadow) is an issue that requires extra attention. As such, Wu[59] has proposed a normalized spectral mixture analysis (NSMA), which can effectively eliminate the shadow endmembers and reduce the intraendmember spectral variability.[60] The algorithms of the NSMA model are as follows:

$$\overline{R_b} = \frac{R_b}{\mu} \times 100, \tag{8}$$

$$\mu = \frac{1}{N} \sum_{b=1}^{N} R_b, \tag{9}$$

where $\overline{R_b}$ is the pixel's normalized reflectance for band b, R_b is the initial reflectance for band b, μ is the mean reflectance for the pixel, and N is the total number of bands. With the normalized spectra, the endmember fractions can be calculated by the full constrained linear spectral mixture analysis:[60]

$$\overline{R_b} = \sum_{i=1}^{N_E} f_i \overline{R_{i,b}} + e_b, \tag{10}$$

$$\sum_{i=1}^{N_E} f_i = 1, \qquad f_i \geq 0, \tag{11}$$

where i is the type of each endmember ($i = 1$, 2, 3, and 4 refer to the endmembers of vegetation, soil, high- and low-albedo, respectively), N_E is the number of the endmembers, f_i is the fraction of endmember i, $\overline{R_{i,b}}$ is the reflectance of the endmember i in band b for the pixel, and e_b is the residual, respectively.

The vegetation component fraction (f_v), the soil component fraction (f_s), and the high- and low-albedo fractions ($f_{imp,h}$ and $f_{imp,l}$) can be extracted by the NSMA model, which has provided important parameters including the proportions of vegetation, soil, and also of impervious surface for estimating urban ET.

3.1.3 *Improving the calculation of the vegetation component latent heat flux*

A parallel SEB model considers vegetation transpiration and soil evaporation as two independent and parallel processes in land surface ET.[41] This type of model is generally applied to areas where vegetation is sparsely and unevenly distributed, e.g., an urban context. In addition, land surface parameters required for the parallel SEB models can be easily acquired through remote sensing images without taking into account the coupling effect between vegetation and soil. Therefore, based on the parallel SEB models, Zhang et al.[39] have proposed a modified multisource parallel model that defines the SEB relationship of each land surface component in urban areas. The component SEB equation of vegetation component in a mixed pixel can be expressed as follows:

$$\lambda E_v = R_{n,v} - H_v, \tag{12}$$

where $R_{n,v}$ is the component net radiant flux of vegetation, H_v is the sensible heat flux of vegetation, and λE_v is the component latent heat flux of vegetation.[39] According to the study by Zhang et al.,[39] $R_{n,v}$ in a mixed pixel can be expressed as f_v multiplied by the net radiation $R_{n,v}^*$ in a hypothetical pure pixel called P1, in which the vegetation fraction is 100%, and all the conditions of the surface and environment are the same as the vegetation component in the mixed pixel. In addition, H_v in a mixed pixel can also be expressed as f_v multiplied by the sensible heat flux H_v^* in the hypothetical pure pixel P1. Therefore, Eq. (12) can be transformed into

$$\lambda E_v = f_v R_{n,v}^* - f_v H_v^* = f_v \times \lambda E_v^*, \tag{13}$$

where λE_v^* is the latent heat flux of the hypothetical pure pixel of vegetation. The component latent heat flux of vegetation in a mixed pixel can be calculated as follows by combining Eqs. (13) and (3) (with F_C being set at 1):

$$\lambda E_v = f_v \left[\frac{\Delta R_{n,v}^* + \rho C_p (e_s - e_a)/r_{ah,v}}{\Delta + \gamma \left(1 + \frac{r_{s,v}}{r_{ah,v}}\right)} \right], \tag{14}$$

where $r_{ah,v}$ is the aerodynamic resistance of vegetation.

3.1.4 *Improving the calculation of soil component latent heat flux*

The component SEB equation of the soil component in a mixed pixel can be expressed as follows:[39]

$$\lambda E_s = R_{n,s} - H_s - G_s, \tag{15}$$

where $R_{n,s}$ is the component net radiant flux of soil, H_s is the component sensible heat flux of soil, λE_s is the component latent heat flux of soil,[39] and G_s is the soil heat flux of the soil component.

The derivation of the component latent heat flux of soil is similar to that of vegetation. $R_{n,s}$ in a mixed pixel can be expressed as f_s multiplied by the net radiation $R_{n,s}^*$ in a hypothetical pure pixel called P2, in which the soil fraction is 100% and all the conditions of surface and environment are the same as the soil component in the mixed pixel; H_s in a mixed pixel can be expressed as f_s multiplied by the sensible heat flux H_s^* in the hypothetical pure pixel P2; and G_s in a mixed pixel can be expressed as f_s multiplied by the soil heat flux G_s^* in the hypothetical pure pixel P2. Therefore, Eq. (15) can be transformed into the following:

$$\lambda E_s = f_s R_{n,s}^* - f_s H_s^* - f_s G_s^* = f_s \times \lambda E_s^*, \tag{16}$$

where λE_s^* refers to the latent heat flux of the hypothetical pure pixel of soil. The component latent heat flux of soil in a mixed pixel can be calculated as follows by combining Eqs. (16) and (4) (with F_C being set at 0):

$$\lambda E_s = f_s \left[\frac{\Delta(R_{n,s}^* - G_s^*) + \rho C_p(e_s - e_a)/r_{ah,s}}{\Delta + \gamma\left(1 + \frac{r_{\text{tot}}}{r_{ah,s}}\right)} \times \left(\frac{\text{RH}}{100}\right)^{(e_s - e_a)/100} \right], \qquad (17)$$

where $r_{ah,s}$ refers to the aerodynamic resistance of soil.

3.1.5 Algorithm of the urban evapotranspiration

As previously mentioned in Secs. 3.1.3 and 3.1.4, urban ET can be estimated as the combination of Eqs. (14) and (17), which can be expressed as follows:

$$\lambda E_{\text{urban}} = \lambda E_v + \lambda E_s$$
$$= f_v \left[\frac{\Delta R_{n,v} + \rho C_p(e_s - e_a)/r_{ah,v}}{\Delta + \gamma\left(1 + \frac{r_{s,v}}{r_{ah,v}}\right)} \right]$$
$$+ f_s \left[\frac{\Delta(R_{n,s} - G_s) + \rho C_p(e_s - e_a)/r_{ah,s}}{\Delta + \gamma\left(1 + \frac{r_{s,s}}{r_{ah,s}}\right)} \times \left(\frac{\text{RH}}{100}\right)^{(e_s - e_a)/100} \right], \qquad (18)$$

where λE_{urban} refers to the total ET of an urban area and ρ (kg · m^{-3}). Note that e_s (Pa), e_a (Pa), and RH (%) can be obtained or calculated by the meteorological data. The other parameters include f_v and f_s, $r_{ah,v}$ and $r_{ah,s}$, $r_{s,v}$ and $r_{s,s}$, $R_{n,v}$ and $R_{n,s}$, and G_s, which are five types of major parameters that can be calculated from remote sensing data.

3.2 Linear Spectral Mixture Analysis

To better illustrate the calculation process of the urban RS-PM model, four flowcharts detailing the input data, intermediate parameters, formulas, and output results are given in different sections of this paper. The flowchart of the first step (Secs. 3.2 to 3.4) of the calculation process of our model is shown in Fig. 3, which demonstrates the estimation process of component fractions and temperatures.

3.2.1 Linear spectral unmixing

According to Sec. 3.1.2, in the linear spectral mixture analysis, the NSMA model was first applied to eliminate the shadow endmembers and reduce the intraendmember spectral variability.[60] Then, the pure pixel index method[39] was used to extract the endmembers of vegetation, soil, high-, and low-albedo in mixed pixels. Because open water body is hardly mixed with other components, water was masked out through the land cover classification before endmember selection.[55] The fraction of each endmember was inversed in the fully constrained LSMA model using a least squares method.[60]

As an important parameter in the urban RS-PM model, the component fractions of vegetation and soil directly determine the proportion of the ET in a mixed pixel. Therefore, high accuracy of component fraction estimation should be ensured. For the fully constrained LSMA model, the modeling accuracy can be assessed by the RMS[55] over all image bands:

$$RMS = \left(\sum_{b=1}^{N} e_b/N \right)^{0.5}, \qquad (19)$$

where e_b is the residual in the calculation of band b, and N is the number of all bands involved in linear spectral unmixing. The RMS results for the eight Landsat 8 images are shown in Table 5. The average RMS of each scene was <0.02, indicating good LSMA accuracy.[55]
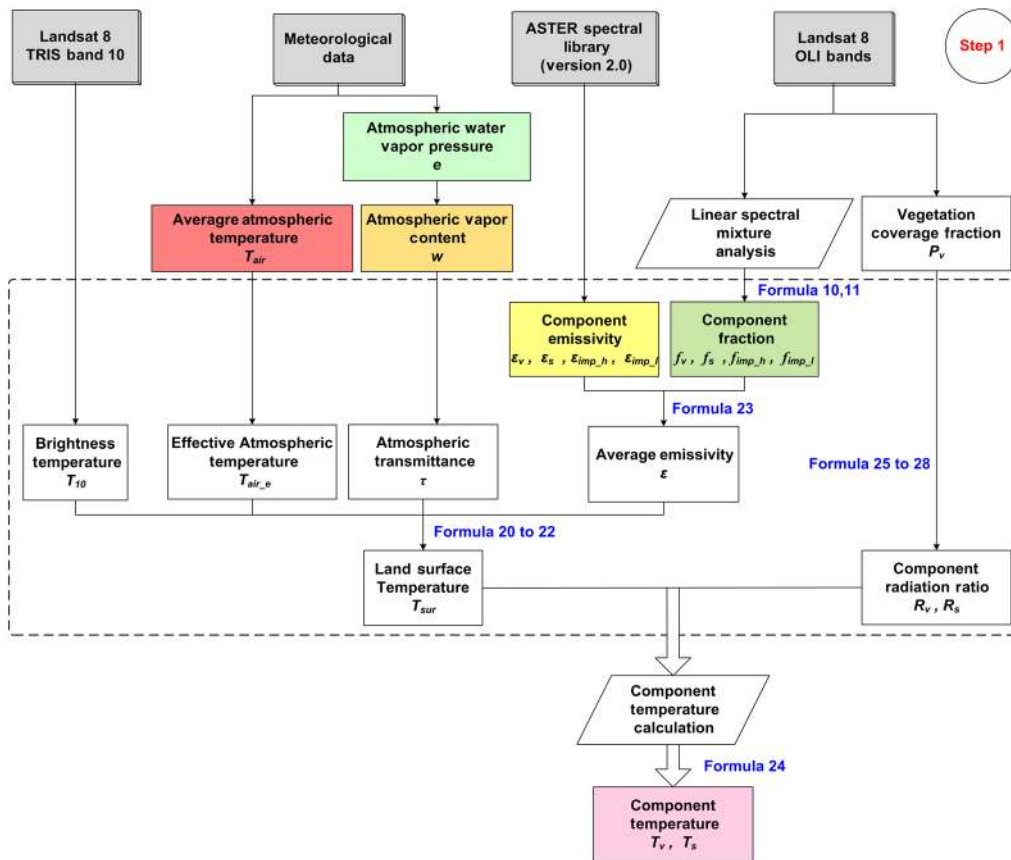
Fig. 3 Flowchart of the first step (step 1) of the urban RS-PM model, detailed in Secs. 3.2–3.4. The gray rectangles represent the input data, and the other color rectangles indicate the parameters that were used more than once in the next steps. Equations used in each of the processes are highlighted in blue.

Table 5 Average RMS for each fully constrain LSMA.

Landsat 8 image (acquisition date)	Average RMS
May 01, 2014	0.0090
October 24, 2014	0.0104
December 21, 2015	0.0080
February 16, 2016	0.0117
March 10, 2016	0.0129
September 02, 2016	0.0098
September 04, 2016	0.0104
November 05, 2016	0.0084

3.2.2 Accuracy assessment of component fractions

The modeled component fractions were assessed by high-resolution Gaofen image data (Table 2). A total of 100 validation samples, each consisting of 3×3 pixels (90×90 m) in Landsat 8 imagery, were randomly generated, and the actual component fractions of each validation sample were extracted from the GF-1 or GF-2 images through visual interpretation.
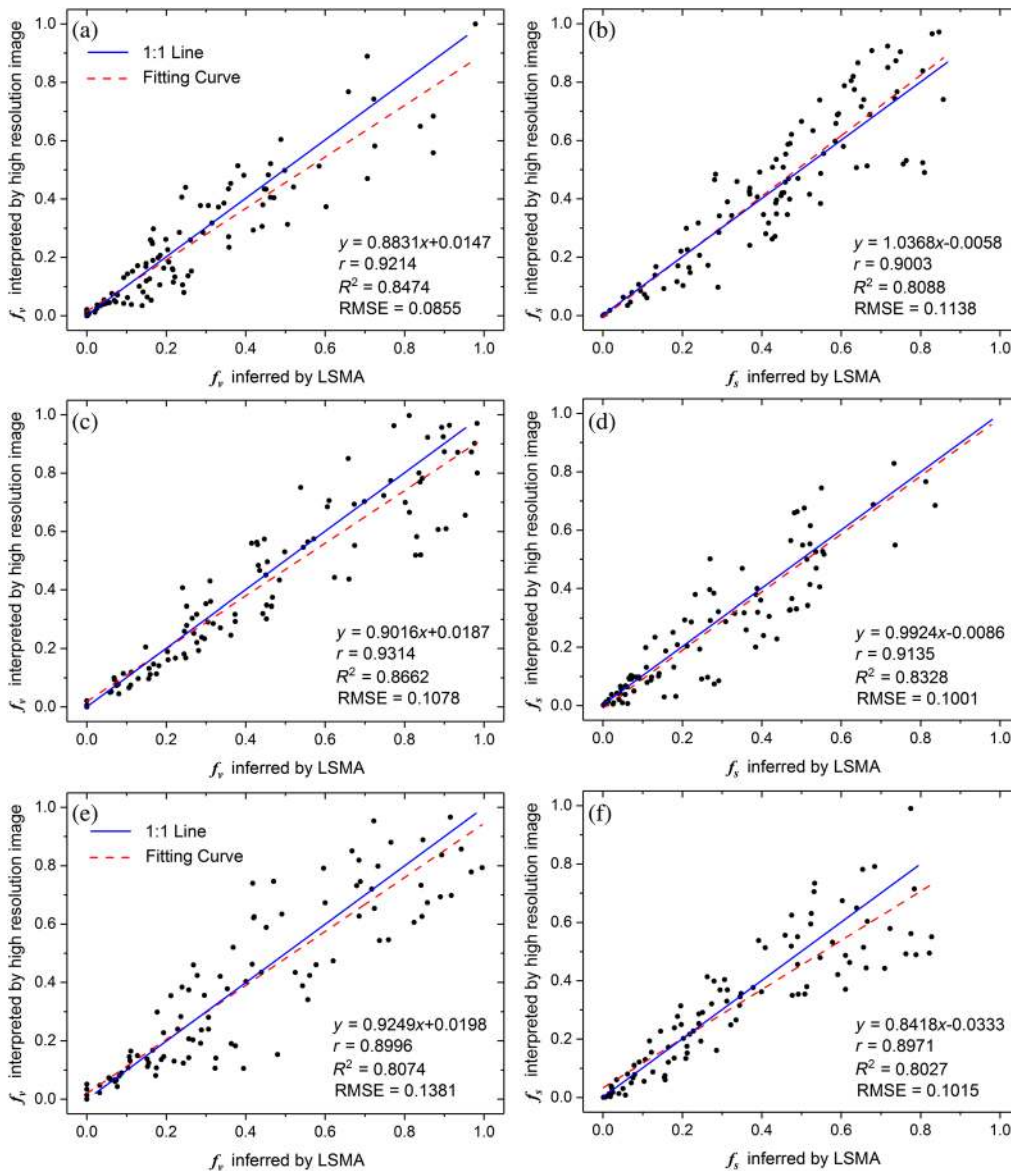
Fig. 4 Comparing the modeled component fractions with the actual fractions derived from the high-resolution Gaofen image data: (a), (c), (e) vegetation fractions inferred from the September 24, 2014, September 04, 2016, and November 05, 2016 Landsat 8 images; (b), (d), and (f) soil fractions inferred from the September 24, 2014, September 04, 2016, and November 05, 2016 Landsat 8 images.

As only the component fractions of vegetation and soil were used in the calculation of ET, we examined only the accuracies of estimating vegetation and soil fractions. Scatter plots (Fig. 4) between the modeled and the actual component fractions show high correction coefficients (both ∼0.9) and low root-mean-square error (RMSEs) (both approximately 0.1). These indicate that the LSMA produced good surface component fractions, which are acceptable and allowed for the following calculations.

3.3 Inversion of Land Surface Temperature

Following LSMA, we then immediately inferred the land surface temperature from the Landsat 8 data as it is an intermediate parameter for obtaining the component surface temperature, the component net radiation, and the aerodynamic resistance. Based on the monowindow algorithm proposed by Qin et al.,[61] Wang et al.[62] have developed an improved monowindow

algorithm for inferring the land surface temperature from Landsat 8 data, which can be expressed as follows:

$$T_{\text{sur}} = \{a(1 - C - D) + [b(1 - C - D) + C + D]T_{10} - DT_{\text{air}\_e}\}/C, \qquad (20)$$

$$C = \varepsilon\tau, \qquad (21)$$

$$D = (1 - \tau)[1 + (1 - \varepsilon)\tau], \qquad (22)$$

where T_{sur} is the land surface temperature, a and b are the linear regression coefficients of Plank function for TIRS band 10, T_{10} is the brightness temperature of Landsat 8 TIRS band 10, T_{air_e} is the effective mean atmospheric temperature, and τ is the atmospheric transmittance of Landsat 8 TIRS band 10, which can be estimated by its relationship with water vapor content proposed by Wang et al.[39,62] Note that ε is the land surface emissivity for Landsat 8 TIRS band 10, which can be estimated with the following equation:[39]

$$\varepsilon = f_v R_v \varepsilon_v + f_s R_s \varepsilon_s + f_{\text{imp},h} R_{\text{imp}} \varepsilon_{\text{imp},h} + f_{\text{imp},l} R_{\text{imp}} \varepsilon_{\text{imp},l}, \qquad (23)$$

where R_v, R_s, and R_{imp} refer to the ratio of component radiation to average radiation in a mixed pixel with $R_i = (T_i/T_{\text{sur}})^4$ (i refers to the components of vegetation, soil, high-, or low-albedo);[61] and ε_v, ε_s, $\varepsilon_{\text{imp},h}$, and $\varepsilon_{\text{imp},l}$ refer to the component typical emissivity, which can be obtained from the ASTER Spectral Library.[39,63]

3.4 Estimation of Component Surface Temperature

In general, the surface temperatures of the four components (i.e., vegetation, soil, high-, and low-albedo) can be calculated by solving equations established with at least four thermal infrared bands[39]—however, there were only two thermal infrared bands in the Landsat 8 data. According to the definition of component radiation ratio,[61,64] the relationship between the component surface temperature and land surface temperature can be written as follows:

$$T_i = T_{\text{sur}} \times (R_i)^{1/4}. \qquad (24)$$

Qin et al.[61] simulated the relationship between the land surface temperature (T_{sur}) and the vegetation coverage fraction (P_v) in different areas with different pixel mixing ratios, and found that the component radiation ratio has a good linear relationship with P_v, which can be expressed as follows:

$$R_v = 0.9332 + 0.0585P_v, \qquad (25)$$

$$R_s = 0.9902 + 0.1068P_v, \qquad (26)$$

$$R_{\text{imp}} = 0.9886 + 0.1278P_v, \qquad (27)$$

$$P_v = \left(\frac{\text{NDVI} - \text{NDVI}_s}{\text{NDVI}_v - \text{NDVI}_s}\right)^2, \qquad (28)$$

where NDVI_s and NDVI_v refer to the NDVI thresholds values of pure soil and pure vegetation pixels, respectively. Therefore, the component surface temperature can be estimated by combining Eqs. (24)–(28). The accuracy of the component temperatures obtained through this method could be lower than that obtained by solving equations established with four thermal infrared bands;[39] however, the urban RS-PM model is insensitive to the variation of the component surface temperatures (discussed later in Sec. 5), and it is therefore feasible to use the empirical formulas to estimate the component surface temperatures.

3.5 Calculation of Component Aerodynamic Resistance to Heat Transfer

Figure 5 shows the flowchart of the second step (Sec. 3.5) of the urban RS-PM model, which is the calculation process of component aerodynamic resistance.

The component aerodynamic resistance of vegetation and soil can be estimated by the following equations:[39,65]

For unstable conditions with $\forall\, Z/L_M < 0$:

$$r_{ah,i} = \ln\left(\frac{Z - d_{o,i}}{Z_{om,i}} - \psi_m\right) \ln\left(\frac{Z - d_{o,i}}{Z_{oh,i}} - \psi_h\right) / (k_c^2 u_z), \tag{29}$$

$$\psi_m = 2\ln\left(\frac{1+x}{2}\right) + \ln\left(\frac{1+x^2}{2}\right) - 2\arctan(x) + \pi/2, \tag{30}$$

$$\psi_h = 2\ln\left(\frac{1+x^2}{2}\right), \tag{31}$$

$$x = \left[1 - \frac{16(Z-d)}{L_M}\right]^{0.25}, \tag{32}$$

while for stable conditions with $\forall\, Z/L_M > 0$,

$$\psi_m = \psi_h = -5(Z-d)/L_M, \tag{33}$$

where $r_{ah,i}$ is the component aerodynamic resistance of vegetation or soil; Z is the elevation at which the wind speed is observed; $d_{o,i}$ is the component zero displacement heights of vegetation or soil; $Z_{om,i}$ and $Z_{oh,i}$ are, respectively, the roughness lengths for momentum and for heat of vegetation or soil; k_c is the von Karman's constant with $k_c = 0.41$; u_z is the wind speed; ψ_m and ψ_h are, respectively, the stability correction functions for momentum and heat; and L_M is the Monin–Obukhov length that can be estimated as Eqs. (49) and (50)[66] as shown in the Appendix.

For the vegetation component, Brutsaert et al.[67] have modeled an empirical relationship between $Z_{om,v}$, $d_{o,v}$, and the average height of vegetation, which can be expressed as
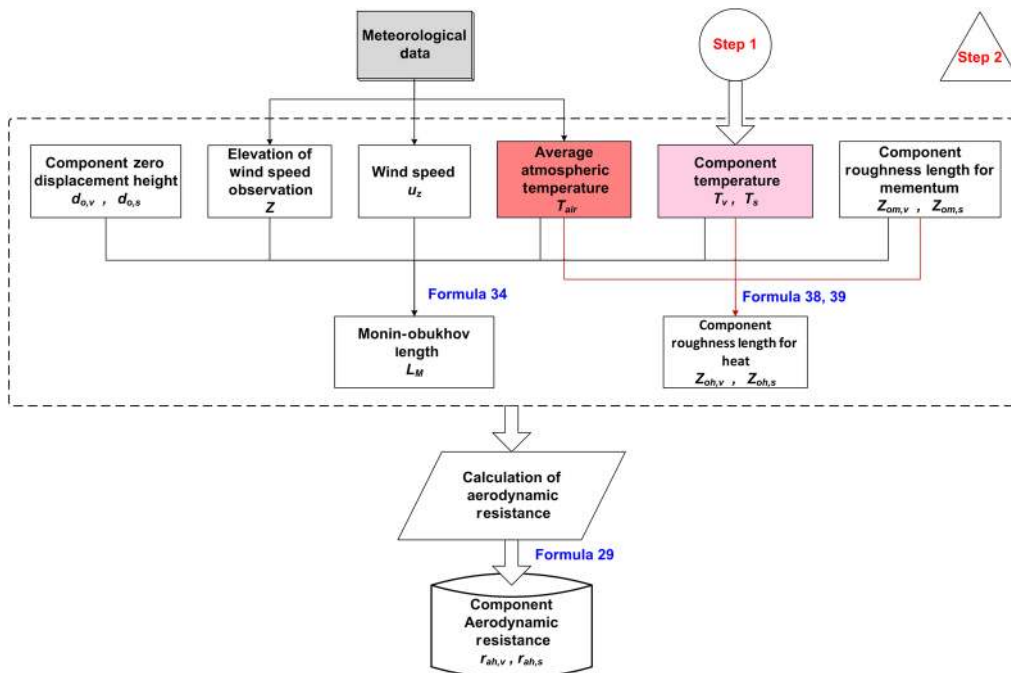

Fig. 5 Flowchart of the second step (step 2) of the urban RS-PM model, detailed in Sec. 3.5.

Eqs. (51) and (52) shown in the Appendix. Kustas et al.[68] have proposed an algorithm for estimating $Z_{oh,v}$, which can be expressed as Eq. (53) shown in the Appendix.

For the soil component, most studies have shown that the roughness for the momentum ($Z_{om,s}$) and the zero displacement height ($d_{o,s}$) of soil are very small and can be taken as constants.[69] According to the measurement of Liu et al.,[70] $Z_{om,s}$ and $d_{o,s}$ were taken as 0.0058 and 0 m, respectively. In addition, $Z_{oh,s}$ can be estimated as Eqs. (54) and (55)[71] shown in the Appendix.

3.6 Calculation of Component Surface Resistance

The flowchart of the third step (Sec. 3.6) of our RS-PM model is shown in Fig. 6, which demonstrates the calculation process of component surface resistance.

For vegetation surface resistance, Mu et al.[23] have proposed to calculate the canopy surface resistance using the stomatal conductance, which can be expressed as follows:

$$g_s = C_L \times m(T_{\min}) \times m(\text{VPD}), \tag{34}$$

$$g_c = g_s \times \text{LAI}, \tag{35}$$

$$r_{s,v} = \frac{1}{g_c}, \tag{36}$$

where g_s is the stomatal conductance, C_L is the potential stomatal conductance per unit LAI, g_c is the canopy stomatal conductance, $r_{s,v}$ is the canopy surface resistance, and $m(T_{\min})$ and $m(\text{VPD})$ are the constraints for minimum air temperature and vapor pressure, respectively, which can be expressed as Eqs. (56) and (57)[23] shown in the Appendix.
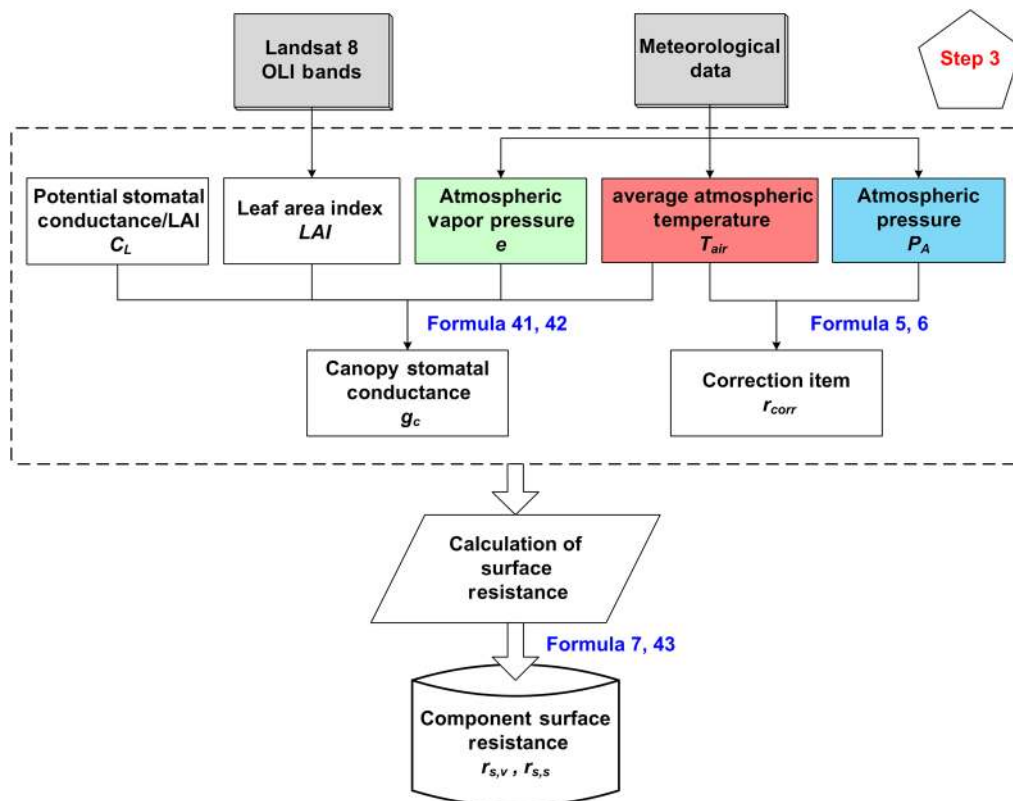

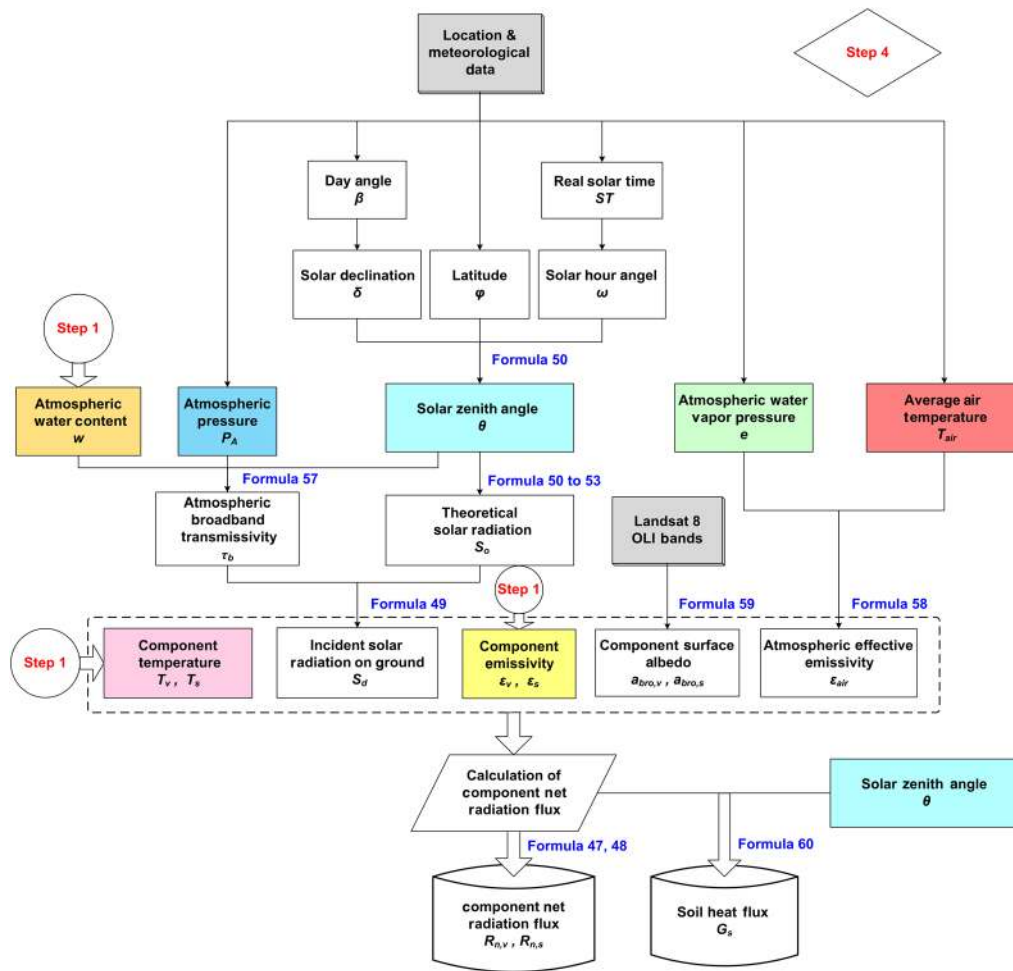**Fig. 6** Flowchart of the third step (step 3) of the urban RS-PM model, detailed in Sec. 3.6.

Fig. 7 Flowchart of the fourth step (step 4) of the urban RS-PM model, detailed in Secs. 3.7–3.8.

3.7 Calculation of the Component Net Radiation Flux

The flowchart of the fourth step (Secs. 3.7–3.8) of our model, which is the calculation processes for component net radiation flux and soil heat flux, is shown in Fig. 7.

3.7.1 Algorithm of the component net radiation flux

The net radiation flux is the sum of net shortwave radiation and net longwave radiation received by land surface, which can be given by the following equation:[22,42,72]

$$R_n = (1 - a)S_d + \varepsilon_{air}\sigma T_{air}^4 - \varepsilon\sigma T_{sur}^4, \tag{37}$$

where a is the land surface albedo, S_d is the incident solar radiation on ground, ε_{air} is the effective emissivity of the atmosphere, and σ is the Stefan Boltzmann constant with $\sigma = 5.67 \times 10^{-8}$ W $\cdot$ m^{-2} $\cdot$ K^{-4}. Based on Eq. (37), Zhang et al.[39] have proposed a new algorithm for calculating the component net radiation flux of vegetation and soil, which can be expressed as follows:

$$R_{n,v} = (1 - a_v)S_d + \varepsilon_{air}\sigma T_{air}^4 - \varepsilon_v\sigma T_v^4, \tag{38}$$

$$R_{n,s} = (1 - a_s)S_d + \varepsilon_{air}\sigma T_{air}^4 - \varepsilon_s\sigma T_s^4, \tag{39}$$

where $R_{n,v}$ and $R_{n,s}$ refer to the component net radiation flux of vegetation and soil, respectively; a_v and a_s refer to the land surface albedos of vegetation and soil, respectively; ε_v and ε_s refer to

the component typical emissivity of vegetation and soil, respectively; and T_v and T_s refer to the component surface temperature of vegetation and soil, respectively.

3.7.2 *Algorithm of incident solar radiation*

The incident solar radiation S_d contributes mostly to the net radiation flux and largely determines the latent heat and sensible heat fluxes. It is a function of the solar constant I_{sc} (1367 W · m^{-2}), the solar zenith angle θ, the relative Earth–Sun distance d_m, and the atmospheric broadband transmissivity τ_b, which can be expressed as follows:[73,74]

$$S_d = I_{sc} d_m^2 \cos \theta \tau_b, \tag{40}$$

$$\cos \theta = \sin \varphi \sin \delta + \cos \varphi \cos \delta \cos \omega, \tag{41}$$

where φ is the latitude of the study area, δ is the solar declination, and ω is the solar hour angle. Note that d_m^2, δ, and ω are given by Eqs. (58) to (64)[75] shown in the Appendix.

3.7.3 *Algorithm of atmospheric effective emissivity*

Atmosphere effective emissivity ε_{air} is determined by atmospheric water vapor pressure e and the atmospheric temperature T_{air}. Note that ε_{air} can be estimated as follows under the cloudless condition:

$$\varepsilon_{air} = 1.24(e/T_{air})^{1/7}. \tag{42}$$

3.7.4 *Algorithm of component surface albedo*

Land surface albedo a is the ratio of the solar radiation reflected by the ground to the incident solar radiation. Liang et al.[76] has proposed a linear relationship between the broad albedo and the reflectance in the six bands of Landsat TM/ETM data. Because Landsat 8 OLI data have similar bands, a can be estimated as follows:

$$a_{bro} = 0.366b_2 + 0.130b_4 + 0.373b_5 + 0.085b_6 + 0.072b_7 - 0.0018, \tag{43}$$

where b_x ($x = 2, 4, 5, 6, 7$) is the reflectance in band x of Landsat 8 data. Then, the broad band albedo with the pure pixels of vegetation and soil obtained in LSMA (Sec. 3.2) is overlaid, and the average component surface albedo of vegetation and soil can be obtained, which is shown in Table 6.

3.8 *Calculation of Soil Heat Flux*

Soil heat flux is a part of net radiation energy received and stored by the soil component. Friedl[77] analyzed the relationship between the net radiation flux and the soil heat flux, and reported that the soil heat flux G_s is a function of the component net flux of soil $R_{n,s}$ and the solar zenith angle θ, which can be expressed as follows:

$$G_s = 0.25R_{n,s} \cos \theta. \tag{44}$$

Table 6 Typical albedo of the vegetation and soil components for the study area.

Component	Component albedo
Vegetation	0.18
Soil	0.28

4 Results

4.1 Inversion Results of the Urban Remote Sensing Penman–Monteith Model

To improve calculation efficiency, we coded the urban RS-PM model in the IDL (interface description language) environment. By entering the meteorological data and the intermediate parameters obtained from Secs. 3.2–3.8, the code returned the component transpiration of vegetation (λE_v) and the component evaporation of soil (λE_s) separately and rapidly. By summing λE_v and λE_s [Eqs. (14) and (17)], we obtained the urban surface ET in the study area from 2014 to 2016 (Fig. 8). Because the result was instantaneous ET and had a very small order of magnitude, the latent heat flux LE was used to represent ET.

Pixels with the value of LE > 0 were extracted from the 2014 to 2016 ET maps as shown in Fig. 8, before the statistics on the resultant LE were produced (Table 7).

By overlaying the ET map of each date with the corresponding component fractions of vegetation, soil, and impervious surface, we observed that the characteristics of the spatial distribution of urban surface ET are as follows: (1) the areas with high ET were mainly concentrated in the pixels with high vegetation fractions and had relatively few distributions in the areas with high soil fractions; (2) the areas with low ET were mainly distributed in the pixels with high impervious surface fractions, and the areas with LE = 0 were mainly concentrated in the pure impervious surface pixels; and (3) the average ET was higher in warm months (September 02, 2016, May 01, 2014, October 24, 2014, September 02, 2016, and October 04, 2016) of the study area than in cold months (December 21, 2015, February 16, 2016, March 10, 2016, and November 05, 2016).

4.2 Validation of the Urban Remote Sensing Penman–Monteith Model

Note that the value of a pixel in the ET maps inferred from remote sensing data (Fig. 8) was averaged ET of a geographical area of pixel size (i.e., 30 m × 30 m for Landsat data in this study). Remote sensing inferred ET cannot be directly compared with the ground measured ET for validation due to their different spatial scales[78]—the spatial scale of the ground measured ET is determined by the height of EC, atmospheric stability, wind direction, wind speed, and land surface coverage.[48] To solve this problem, the footprint model[79] was applied in the validation. The contribution of the turbulent flux from the surrounding areas to the ET observation values can be simulated by the footprint model, and the flux footprint (or the source area) $f_{EC}(x, y, z_m)$
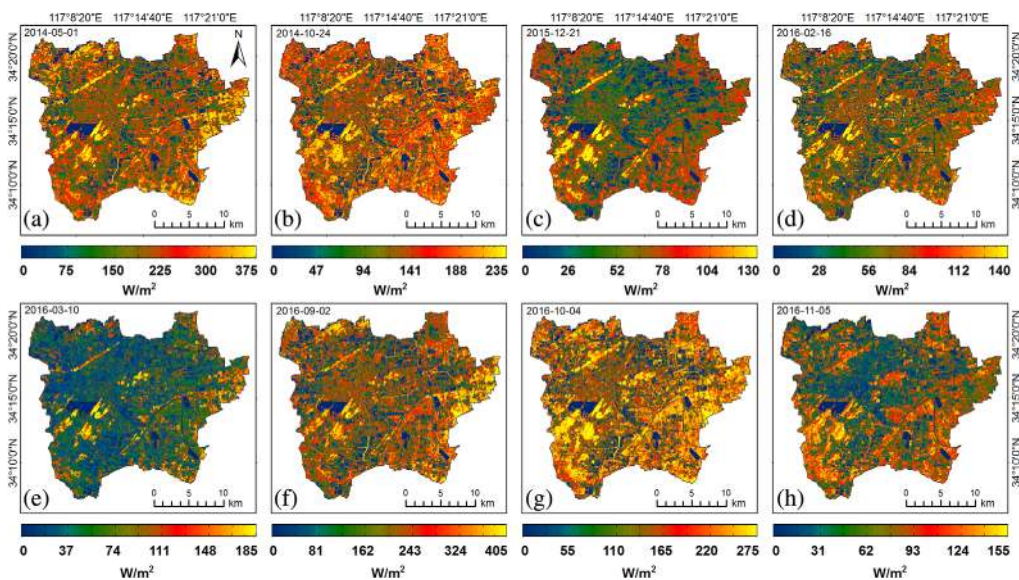

Fig. 8 The urban surface ET (represented by the latent heat flux LE) of the study area from 2014 to 2016 (open water bodies have been masked out and displayed in dark blue in the maps).

Table 7 The statistics on urban surface ET in the study area from 2014 to 2016.

Date	Minimum LE ($W \cdot m^{-2}$)	Maximum LE ($W \cdot m^{-2}$)	Average LE ($W \cdot m^{-2}$)	Standard deviation ($W \cdot m^{-2}$)
May 01, 2014	0.01049	373.54	206.13	80.16
October 24, 2014	0.00024	234.66	147.26	51.37
December 21, 2015	0.00015	130.26	60.01	29.34
February 16, 2016	0.00100	137.72	71.32	31.33
March 10, 2016	0.00161	182.02	61.11	42.67
September 02, 2016	0.00210	402.23	209.14	104.54
September 04, 2016	0.00058	272.21	174.80	71.57
November 05, 2016	0.00042	151.40	71.28	39.00

of the ET observation can be obtained.[80–82] The Eulerian analytic footprint model can be expressed as follows:[79]

$$f_{EC}(x, y, z_m) = D_y(x, y)f^y(x, z_m), \tag{45}$$

where x is the downwind distance pointing against the average horizontal wind direction, y is the lateral wind distance, z_m is the height of EC observation, $f^y(x, z_m)$ is the lateral wind integral footprint function, and $D_y(x, y)$ is the Gaussian lateral wind spread function.[48] Figure 9 shows the source area with contribution weights for the EC measurements simulated by the footprint model.

After obtaining the spatial distributions and the contribution weights of the source areas, we calculated the ET weighted average of all pixels in the source area by the following equation:

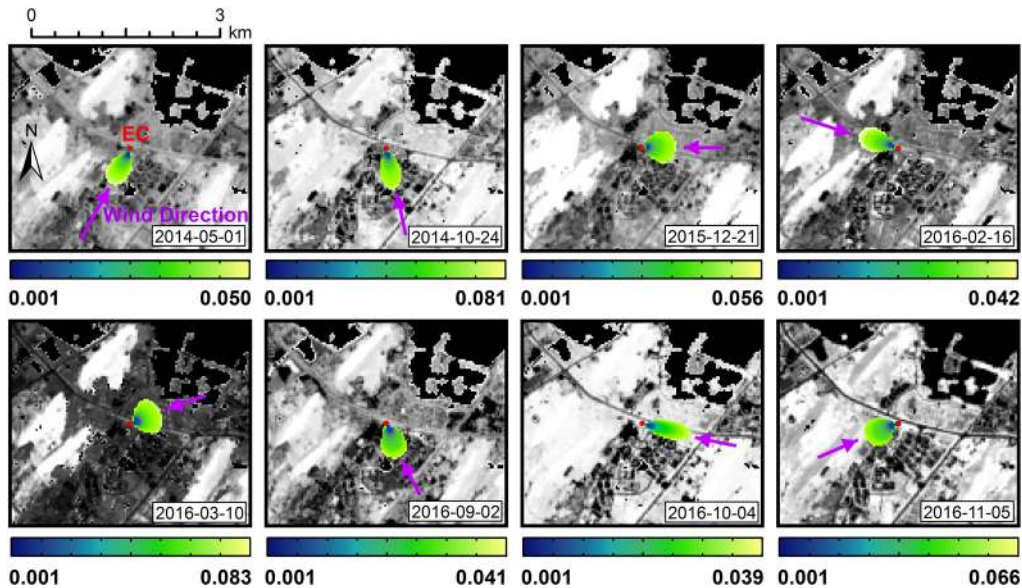$$LE_F = \sum_{i=1}^{n}(x_i \times LE_i), \tag{46}$$

Fig. 9 Schematic diagrams of remote sensed ET (gray-scale images) overlaid with the source areas (colorful areas) of EC from 2014 to 2016. Purple arrows indicate wind directions for different dates.
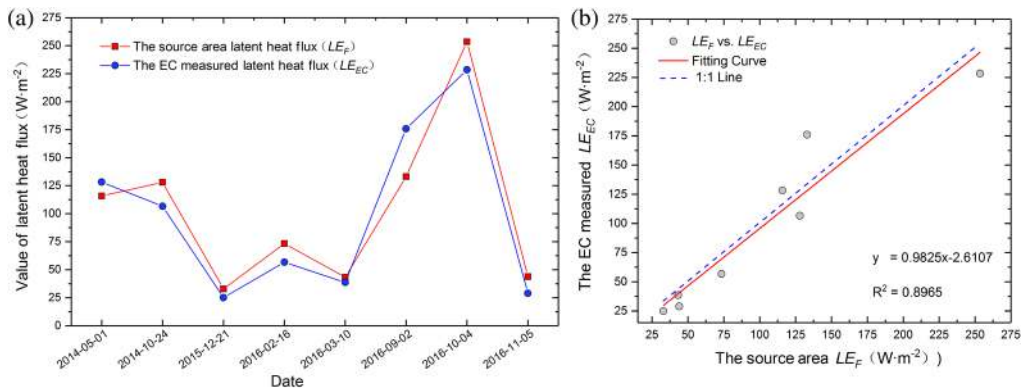
Fig. 10 (a) Variation trends comparison between the source area LE_F and the EC measured LE_{EC}; and (b) scatterplot of the source area LE_F against the EC measured LE_{EC}. The source area LE_F agrees well with the EC measured LE_{EC}.

where LE_F is the weighted average value of the latent heat flux in the source area (henceforth referred to as the source area latent heat flux), which has the same spatial scale with the latent heat flux measured by ground EC (LE_{EC}); x_i is the value of contribution weight for pixel i in the source area, n is the total number of the pixels in the source area, and LE_i is the latent heat flux inferred by remote sensing data for pixel i. The differences and variation trends of the source latent heat flux LE_F and the measured latent heat flux LE_{EC} for the eight dates are shown in Fig. 10(a). It is shown that the variation trends of the source area LE_F and the EC measured LE_{EC} were basically consistent with each other.

Table 8 shows the statistics on the difference between LE_F and LE_{EC} for the eight dates: the maximum error and the maximum error rate were -42.85 W $\cdot$ m^{-2} (September 02, 2016) and 52.11% (November 05, 2016), respectively, and the minimum error and the minimum error rate were 4.52 W $\cdot$ m^{-2} (March 10, 2016) and 9.67% (May 01, 2014), respectively. Our comparative analysis indicates that the ET inferred by the urban RS-PM model is acceptable in general.

To further evaluate the accuracy of the ET inferred by the urban RS-PM model, three error assessment indices were used here: the RMSE, which reflects the dispersion degree of the inferred value to the measured value; the mean relative error (MRE), which reflects the relative deviation degree of the inferred value from the measured value; and the correlation coefficient (r), which reflects the similarity degree between the variation trends of the inferred value and the measured value. Equations for calculating these indices are expressed as Eqs. (65)–(67) in the Appendix. The results of accuracy assessment showed that the RMSE, MRE, and r are

Table 8 Error statistics on the source area LE_F in relation to the EC measured LE_{EC}.

Date	LE_F (W $\cdot$ m^{-2})	LE_{EC} (W $\cdot$ m^{-2})	Error $LE_F - LE_{EC}$ (W $\cdot$ m^{-2})	Error rate (%)
May 01, 2014	115.84	128.25	-12.41	9.67
October 24, 2014	127.97	106.57	21.40	20.08
December 21, 2015	32.91	24.99	7.92	31.69
February 16, 2016	73.39	56.72	16.67	29.39
March 10, 2016	43.19	38.67	4.52	11.68
September 02, 2016	133.03	175.88	-42.85	24.36
September 04, 2016	253.52	228.47	25.05	10.97
November 05, 2016	43.90	28.86	15.04	52.11

24.14 W · m^{-2}, 18.5%, and 0.9546, respectively. By plotting the source area LE$_F$ against the EC measured LE$_{EC}$ and fitting them [Fig. 10(b)], we noticed that the fitting line was very close to the 1:1 line, and that the goodness of the linear fitting result R^2 was 0.8965. This further proves that the urban RS-PM model can estimate reliable urban ET at high accuracy.

5 Discussion

5.1 Parameter Sensitivity Analyses

5.1.1 Sensitivity analyses of component fractions

Compared with the parameters in the traditional RS-PM model, four major parameters have been included in the urban RS-PM model, namely the component fractions of vegetation f_v and of soil f_s, and the component net radiation flux of vegetation $R_{n,v}$, and of soil $R_{n,s}$. It is necessary to analyze how sensitive the RS-PM model is to the variations of these parameters. Based on Eqs. (38) and (39), for a given remote sensing image, a_v, a_s, ε_v, and ε_s are constants, and S_d and T_{air} are affected mainly by the acquisition time of the remote sensing image data, the location of the study area, and the local meteorology. Therefore, $R_{n,v}$ and $R_{n,s}$ are determined mainly by the component surface temperatures T_v and T_s. According to Eq. (24), T_v and T_s are calculated by T_{sur}—$R_{n,v}$ and $R_{n,s}$, therefore, can be represented by T_{sur} for sensitivity analysis.

The modeled ET of October 24, 2014, is used as the reference data for sensitivity analysis. For the sensitivity analysis of f_v and f_s, we assume that all other parameters are stable when the controlled variable changes.[39] In the component fraction image of vegetation (or soil), a change ranging from −0.3 to 0.3 with an increase of 0.1 in f_v (or f_s) is set, and four testing areas with the initial f_v (or f_s) values between 0.3 to 0.4, 0.4 to 0.5, 0.5 to 0.6, and 0.6 to 0.7, respectively, were selected for sensitivity analysis. As the sum of the component fractions in a pixel is one for the fully constrained LSMA [i.e., Eq. (11)], each time when f_v (or f_s) changes, the variation value of f_v (or f_s) should be assigned to the other components based on the initial proportions of each component, which can be expressed as follows (using f_v variation as an example):

$$f_{v\_va} = f_{v\_ini} + \Delta f_v, \tag{47}$$

$$f_{s\_as} = f_{s\_ini} - \Delta f_v \left(\frac{f_{s\_ini}}{f_{s\_ini} + f_{imp,h\_ini} + f_{imp,l\_ini}} \right), \tag{48}$$

where f_{v_va} is the vegetation component fraction after adding a change value of Δf_v; f_{s_as} is the soil component fraction when the vegetation component fraction obtains an addition of Δf_v; and f_{v_ini}, f_{s_ini}, f_{imp,h_ini}, and f_{imp,l_ini} are the initial component fractions of vegetation, soil high- and low-albedo impervious surface, respectively. The average value of the corresponding ET in each testing area for each change of f_v (or f_s) is recorded and shown in Fig. 11.

Figure 11 shows that the resultant ET is positively linearly correlated with the variation value of vegetation or the soil fraction. However, the RS-PM model is more sensitive to the variation of vegetation fraction as large slopes can be observed for the fitting lines in Fig. 11(a). Table 9 shows that as the vegetation fraction increases by 0.1, the growth rates of the average corresponding ET in the four testing areas are 8.28%, 7.95%, 7.85% and 8.02%, respectively; as soil fraction increases by 0.1, the average growth rates of the corresponding ET in the four testing areas are 0.23%, 0.45%, 0.66%, and 0.66%, respectively. These indicate that the vegetation fraction has a greater influence on the ET estimation by the urban RS-PM model.

5.1.2 Sensitivity analysis of land surface temperature

As the urban RS-PM model is proven sensitive by its variation, we control the f_v value within a certain range to reduce its effect on the result of the sensitivity analysis of T_{sur}. In the land surface
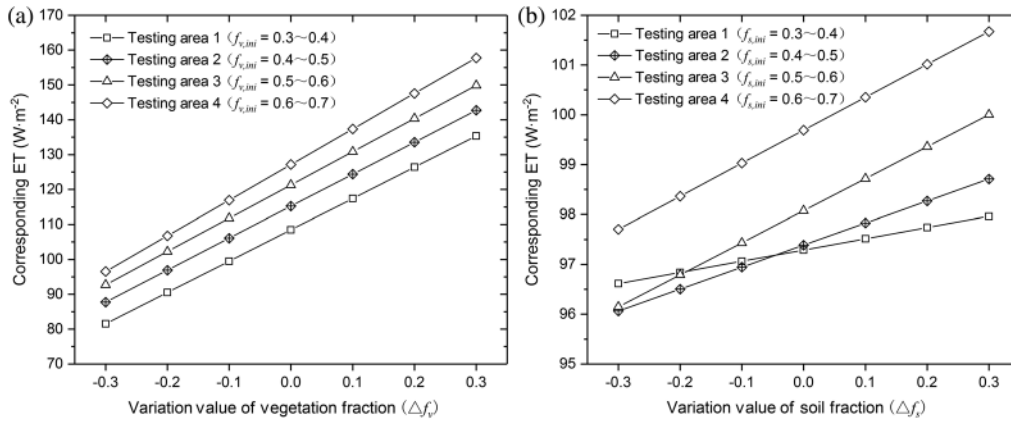
Fig. 11 Sensitivity of the RS-PM model with the variation of (a) vegetation fraction and (b) soil fraction.

Table 9 Statistics of the variation rates of the corresponding ET for Δf_v or Δf_s.

	Testing area							
	Variation rate of corresponding ET for Δf_v (%)				Variation rate of corresponding ET for Δf_s (%)			
Δf_v or Δf_s	1	2	3	4	1	2	3	4
−0.3	24.83	23.85	23.56	24.07	0.69	1.36	1.97	1.99
−0.2	16.55	15.90	15.71	16.05	0.46	0.91	1.31	1.33
−0.1	8.28	7.95	7.85	8.02	0.23	0.45	0.66	0.66
0.1	−8.28	−7.95	−7.85	−8.02	−0.23	−0.45	−0.66	−0.66
0.2	−16.55	−15.90	−15.71	−16.05	−0.46	−0.91	−1.31	−1.33
0.3	−24.83	−23.85	−23.56	−24.07	−0.69	−1.36	−1.97	−1.99

temperature image of October 24, 2014, we first extract the total testing area with the f_v value that was limited to the range of 0.45 to 0.55 (the following four testing areas were extracted from the total testing area). A change ranging from −5 to 5 K with an increase interval of 1 K was set, and the four testing areas with the initial T_{sur} value from 295 to 296 K, 298 to 299 K, 301 to 302 K, and 304 to 305 K, respectively, were selected from the extracted areas for sensitivity analysis. The average value of the corresponding ET of each testing area for each change of T_{sur} is recorded and shown in Fig. 12.

Figure 12 shows that there is a negative correlation between the corresponding ET and the variation value of the land surface temperature and that the corresponding ET is less sensitive to the variation of the land surface temperature. Table 10 shows that as the land surface temperature increases by 1 K, the mean growth rates of the average corresponding ET of the four testing areas are appropriately −0.37%, −0.31%, −0.58%, and −0.65%, respectively. This indicates that the variation of the land surface temperature has less influence on the ET estimation by the urban RS-PM model—the urban RS-PM model is not that sensitive to this parameter. As such, it is acceptable to use the empirical algorithm for estimating the component temperatures (Sec. 3.4) even if the estimations are not that accurate.

5.2 *Accuracy Assessment*

As previously mentioned, urban ET estimations remain scarce and we here compare our urban RS-PM model with other remote sensing-based ET estimation models for natural surfaces. In our
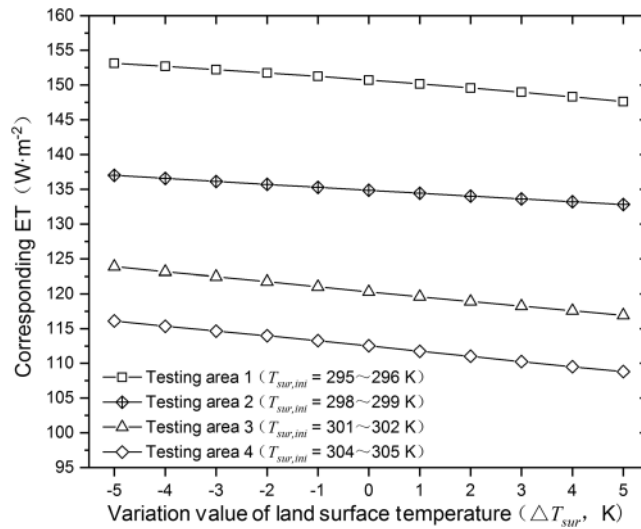
Fig. 12 Sensitivity of the RS-PM model with the variation of land surface temperature.

Table 10 Statistics of the variation rates of the corresponding ET for ΔT_{sur}.

	Testing area			
	Variation rate of corresponding ET for ΔT_{sur} (%)			
ΔT_{sur} (K)	1	2	3	4
5	−2.05	−1.50	−2.81	−3.30
4	−1.60	−1.22	−2.27	−2.67
3	−1.16	−0.92	−1.72	−2.02
2	−0.76	−0.62	−1.16	−1.33
1	−0.37	−0.31	−0.59	−0.69
−1	0.35	0.32	0.60	0.65
−2	0.68	0.63	1.20	1.29
−3	1.00	0.95	1.78	1.88
−4	1.31	1.28	2.37	2.51
−5	1.60	1.60	2.97	3.17

case study of Xuzhou, the urban RS-PM model estimated urban ET with an RMSE of 24.14 W · m^{-2}, an MRE of 18.5%, and a correlation coefficient of 0.9546. This is consistent with the study by Jia et al.[48] who used the footprint model to validate their 30-m resolution ET estimation at different sites and time with the RMSE of 8.99 to 28.07 W · m^{-2}, the r of 0.84 to 0.98, and the MRE of 7.59% to 19.58%, respectively. Some reports[83–85] indicate that most remote sensing-based ET estimations have achieved an MRE ranging from 20% to 30%. Kalma et al.[86] has concluded the accuracy of different remote sensing techniques for estimating ET with an average RMSE of 50 W · m^{-2} and with an MRE of 15% to 30%; the details are shown in Table 11.[86]

Compared with other models, the accuracy ranking of our model is relatively high, thus, it can be concluded that the urban RS-PM model is reasonable and feasible.

Table 11 Accuracy reports of different remote sensing models for estimating ET.

Model	Source	Satellite data	Time step	r	MRE (%)	RMSE (W · m^{-2})
One-source SEB	Su et al.[87]	Mast	30 min	0.92 to 0.94		40 to 47
	McCabe and Wood[88]	ASTER	Instant	0.81 to 0.87		68 to 99
Two-source SEB	Kustas and Norman[89]	Masts and aircraft	Instant		12 to 15	37 to 47
	Norman et al.[90]	Masts	30 min		27	105
	Li et al.[91]	Landsat 7 ETM Landsat 5 TM	30 min		10 to 15	50 to 55
T_{rad}-VI	Gillies et al.[92]	Aircraft	Satellite transit time	0.89 to 0.95	10 to 30	25-55
	Jiang and Islam[93,94]	AVHRR	Satellite transit time	0.80 to 0.95	15 to 30	59-85
ALEXI	Anderson et al.[95]	GOES and MODIS	Satellite transit time		25	58
SEBAL	French et al.[96]	ASTER	30 min		15	55
S-SEBI	Verstraeten et al.[97]	AVHRR	30 min		24	35
Empirical method	Wang et al.[98]	MODIS	16 days	0.90	36	32

6 Conclusions

As an algorithm that was developed particularly for estimating the ET of urban areas with a heterogeneous underlying surface, our urban RS-PM (remote sensing Penman–Monteith) model has made three major modifications based on the traditional RS-PM model: (1) the interference of impervious surface components in urban areas was excluded, using the component fractions of vegetation and soil extracted through linear spectral mixture analysis to replace the vegetation cover fraction index, which can accurately calculate the proportions of vegetation and soil; (2) the component latent heat flux was estimated by the modified multi-source parallel model, which considered the effect of the component fraction on all energy components in the SEB; and (3) the calculation of the component net radiation flux was optimized by considering the component surface characteristics. In addition, an empirical approach was included in the urban RS-PM model to simplify the calculation of component temperatures.

The successful application of the urban RS-PM model in the case study of Xuzhou, which achieved an acceptable accuracy, proves that our model is effective in estimating urban ET. Parameter sensitivity analyses indicated that both vegetation and soil component fractions are important parameters in the RS-PM model, which is more sensitive to the vegetation component fraction than to the soil component fraction. It is noted that the model is insensitive to the component land surface temperature, which justifies the use of the empirical algorithm for estimating the component temperature.

Due to the discontinuity of the EC observations, only eight appropriate Landsat 8 images of the study area can be selected during the observation periods in this study, which may weaken our validation compared with the validation based on more samples. Future work should investigate the applicability and robustness of the urban RS-PM model on areas at the regional and national scales using lower-resolution image data.

7 Appendix: Equations of the Intermediate Parameters

$$L_M = u_*^2 T_{\text{air}}/k_c g T_*,\qquad(49)$$

$$u_* = \frac{k_c u_z}{\ln[(Z-d)/Z_{om,i}]},\qquad(50)$$

where u_* is the friction velocity, g is the gravitational acceleration with $g = 9.8\ \text{m} \cdot \text{s}^{-2}$, and T_* is the temperature scale with $T_* = T_{\text{sur}} - T_{\text{air}}$:

$$Z_{om,v} = h_v/8,\qquad(51)$$

$$d_{o,v} = 2h_v/3,\qquad(52)$$

where h_v is the average height of vegetation; in urban areas, h_v can be given a value of 5 m:[39]

$$Z_{oh,v} = Z_{om,v} e^{-S_{kb} u_z |T_v - T_{\text{air}}|},\qquad(53)$$

where T_v is the vegetation component surface temperature and S_{kb} is the empirical coefficient with $S_{kb} = 0.13$:[68]

$$Z_{oh,s} = Z_{om,s} e^{-[2.46(Re_*)^{0.25}-2]},\qquad(54)$$

$$Re_* = \frac{u_* Z_{om,s}}{v},\qquad(55)$$

where Re_* is the roughness Reynolds number and v is the kinematic molecular viscosity with $v = 1.48 \times 10^{-7}\ \text{m}^2 \cdot \text{s}^{-1}$:

$$m(\text{VPD}) = \begin{cases} 1 & \text{VPD} \le \text{VPD}_{\text{open}} \\ \frac{\text{VPD}_{\text{close}} - \text{VPD}}{\text{VPD}_{\text{close}} - \text{VPD}_{\text{open}}} & \text{VPD}_{\text{open}} < \text{VPD} < \text{VPD}_{\text{close}} \\ 0.1 & \text{VPD} \ge \text{VPD}_{\text{close}} \end{cases},\qquad(56)$$

$$m(T_{\min}) = \begin{cases} 1 & T_{\min} \ge T_{\min\_\text{open}} \\ \frac{T_{\min} - T_{\min\_\text{close}}}{T_{\min\_\text{open}} - T_{\min\_\text{close}}} & T_{\min\_\text{close}} < T_{\min} < T_{\min\_\text{open}} \\ 0.1 & T_{\min} \le T_{\min\_\text{close}} \end{cases},\qquad(57)$$

where "close" means nearly complete suppression with full stomatal closure, and "open" means no suppression for transpiration. The threshold values of VPD_{open}, $\text{VPD}_{\text{close}}$, $T_{\min\_\text{open}}$, and $T_{\min\_\text{close}}$ for different biomes have been given in the biome properties look-up table (BPLUT).[23,99] For soil surface resistance, Mu et al.[23] have also proposed an estimation method that is shown as Eqs. (5)–(7):

$$d_m^2 = 1.000110 + 0.034221 \cos\beta + 0.001280 \sin\beta + 0.000719 \cos 2\beta + 0.000077 \sin 2\beta,\qquad(58)$$

$$\delta = 0.006918 - 0.399912 \cos\beta + 0.070257 \sin\beta - 0.006758 \cos 2\beta$$
$$+ 0.000907 \sin 2\beta - 0.002697 \cos 3\beta + 0.00148 \sin 3\beta,\qquad(59)$$

$$\omega = \frac{\pi}{12}(\text{ST} - 12),\qquad(60)$$

where β is the day angle and ST is the real solar time, which can be calculated as follows:[39,100]

$$\beta_d = 2\pi \frac{D_n - 1}{365}, \tag{61}$$

$$ST = h_b + \frac{(\lambda^* - \lambda_s^*) \times 4 + 229.183\eta}{60}, \tag{62}$$

$$\eta = 0.000043 + 0.002061 \cos\theta - 0.032040 \sin\theta - 0.014974 \cos 2\theta - 0.040685 \sin 2\theta, \tag{63}$$

where D_n is the number of days in the year, h_b is the Beijing time (UTC + 8), λ_s^* is the longitude of local standard time (the longitude of Beijing is 120°E), λ^* is the local longitude (the central longitude of the study area is 117.3°E), and η is the time lag (rad).

Long et al.[74] have found incident solar radiation S_d is most sensitive to the variation of the atmospheric broadband transmissivity τ_b, which can be estimated using the model proposed by Allen et al.:[101]

$$\tau_b = 0.35 + 0.627 \exp\left[\frac{-0.00146P_A}{K_t \cos\theta} - 0.075\left(\frac{w}{\cos\theta}\right)\right], \tag{64}$$

where K_t is the atmospheric turbidity coefficient with $0 < K_t \leq 1$: for clean atmosphere $K_t = 1$; and for polluted or turbid atmosphere $K_t = 0.5$:

$$\text{RMSE} = \left[\frac{1}{N}\sum_{i=1}^{N}(\text{LE}_{F,i} - \text{LE}_{\text{EC},i})^2\right]^{0.5}, \tag{65}$$

$$\text{MRE} = \frac{1}{N}\sum_{i=1}^{N}\frac{|\text{LE}_{F,i} - \text{LE}_{\text{EC},i}|}{\overline{\text{LE}_{\text{EC}}}} \times 100\%, \tag{66}$$

$$r = \sum_{i=1}^{N}(\text{LE}_{F,i} - \overline{\text{LE}_F})(\text{LE}_{\text{EC},i} - \overline{\text{LE}_{\text{EC}}}) / \left[\sum_{i=1}^{N}(\text{LE}_{F,i} - \overline{\text{LE}_F})^2 \sum_{i=1}^{N}(\text{LE}_{\text{EC},i} - \overline{\text{LE}_{\text{EC}}})^2\right], \tag{67}$$

where $\text{LE}_{F,i}$ is the source area latent heat flux for each date i ($i = 1$ to 8), $\text{LE}_{\text{EC},i}$ is the EC measured latent heat flux for each date i, N is the total number of the EC measured data with $N = 8$, $\overline{\text{LE}_F}$ is the average source area latent heat flux of all dates, and $\overline{\text{LE}_{\text{EC}}}$ is the average EC measured latent heat flux of all dates.

Acknowledgments

References

1. A. J. Dolman, "Transpiration of an oak forest as predicted from porometer and weather data," *J. Hydrol.* **97**(3–4), 225–234 (1988).
2. K. G. McNaughton and P. G. Jarvis, "Effects of spatial scale on stomatal control of transpiration," *Agric. For. Meteorol.* **54**(2–4), 279–302 (1991).
3. W. R. N. Edwards, "Precision weighing lysimetry for trees, using a simplified tared-balance design," *Tree Physiol.* **1**(2), 127–144 (1986).
4. D. J. Gochis and R. H. Cuenca, "Plant water use and crop curves for hybrid poplars," *J. Irrig. Drain. Eng.* **126**(4), 206–214 (2000).

5. K. B. Wilson et al., "A comparison of methods for determining forest evapotranspiration and its components: sap-flow, soil water budget, eddy covariance and catchment water balance," *Agric. For. Meteorol.* **106**(2), 153–168 (2001).

6. G. Yang et al., "Transformation of surface water and groundwater and water balance in the agricultural irrigation area of the Manas River Basin, China," *Int. J. Agric. Biol. Eng.* **10**(4), 107–118 (2017).

7. J. Jódar et al., "Combination of lumped hydrological and remote-sensing models to evaluate water resources in a semi-arid high altitude ungauged watershed of Sierra Nevada (Southern Spain)," *Sci. Total Environ.* **625**, 285–300 (2018)

8. S. B. Verma, "Micrometeorological methods for measuring surface fluxes of mass and energy," *Remote Sens. Rev.* **5**(1), 99–115 (1990).

9. W. R. Bidlake, W. M. Woodham, and M. A. Lopez, *Evapotranspiration from Areas of Native Vegetation in West-Central Florida*, United States Government Printing Office, Washington, USA (1996).

10. H. A. R. De Bruin, B. J. J. M. Van Den Hurk, and W. Kohsiek, "The scintillation method tested over a dry vineyard area," *Boundary-Layer Meteorol.* **76**(1–2), 25–40 (1995).

11. K. J. McAneney, A. E. Green, and M. S. Astill, "Large-aperture scintillometry: the homogeneous case," *Agric. For. Meteorol.* **76**(3–4), 149–162 (1995).

12. A. Granier, "Une nouvelle methode pour la measure du flux de seve brute dans le tronc des arbres," *Ann. des Sci. For.* **42**(2), 193–200 (1985).

13. A. Granier et al., "Vapour flux density and transpiration rate comparisons in a stand of Maritime pine (Pinus pinaster Ait.) in Les Landes forest," *Agric. For. Meteorol.* **51**(3–4), 309–319 (1990).

14. J. Cermak and N. Nadezhdina, "Sapwood as the scaling parameter—Defining according to xylem water content or radial pattern of sap flow?," *Ann. des Sci. For.* **55**(5), 509–521 (1998).

15. L. Meiresonne et al., "Measured sap flow and simulated transpiration from a poplar stand in Flanders (Belgium)," *Agric. For. Meteorol.* **96**(4), 165–179 (1999).

16. R. G. Allen et al., "Crop evapotranspiration—guidelines for computing crop water requirements," *FAO Irrigation and Drainage*, paper 56 (1998).

17. W. Bastiaanssen et al., "SEBAL model with remotely sensed data to improve water-resources management under actual field conditions," *J. Irrig. Drain. Eng.* **131**(February), 2 (2005).

18. J. L. Monteith, "Evaporation and environment," in *Symposia of the Society for Experimental Biology*, Vol. 19, pp. 205–234 (1965).

19. X. Lu et al., "Partitioning of evapotranspiration using a stable isotope technique in an arid and high temperature agricultural production system," *Agric. Water Manag.* **179**, 103–109 (2017).

20. W. G. M. Bastiaanssen et al., "A remote sensing surface energy balance algorithm for land (SEBAL). 1. Formulation," *J. Hydrol.* **212–213**(1–4), 198–212 (1998).

21. W. G. M. Bastiaanssen et al., "A remote sensing surface energy balance algorithm for land (SEBAL): 2. Validation," *J. Hydrol.* **212–213**(1–4), 213–229 (1998).

22. H. A. Cleugh et al., "Regional evaporation estimates from flux tower and MODIS satellite data," *Remote Sens. Environ.* **106**(3), 285–304 (2007).

23. Q. Mu et al., "Development of a global evapotranspiration algorithm based on MODIS and global meteorology data," *Remote Sens. Environ.* **111**(4), 519–536 (2007).

24. M. Menenti and B. J. Choudhury, "Parameterization of land surface evaporation by means of location dependent potential evaporation and surface temperature range," in *Proc. of IAHS Conf. on Land Surface Processes*, pp. 561–568 (1993).

25. P. H. Gowda et al., "ET mapping for agricultural water management: present status and challenges," *Irrig. Sci.* **26**(3), 223–237 (2008).

26. N. Bhattarai et al., "Utility of remote sensing-based surface energy balance models to track water stress in rain-fed switchgrass under dry and wet conditions," *ISPRS J. Photogramm. Remote Sens.* **133**, 128–141 (2017).

27. Y. Zhou et al., "Assessing the impacts of an ecological water diversion project on water consumption through high-resolution estimations of actual evapotranspiration in the downstream regions of the Heihe River Basin, China," *Agric. For. Meteorol.* **249**, 210–227 (2018).

28. G. J. Roerink, Z. Su, and M. Menenti, "S-SEBI: a simple remote sensing algorithm to estimate the surface energy balance," *Phys. Chem. Earth, Part B Hydrol. Ocean. Atmos.* **25**(2), 147–157 (2000).
29. N. Gaur, B. P. Mohanty, and S. C. Kefauver, "Effect of observation scale on remote sensing based estimates of evapotranspiration in a semi-arid row cropped orchard environment," *Precis. Agric.* **18**(5), 762–778 (2017).
30. Z. L. Li et al., "A review of current methodologies for regional evapotranspiration estimation from remotely sensed data," *Sensors* **9**(5), 3801–3853 (2009).
31. Z. Su, "The Surface Energy Balance System (SEBS) for estimation of turbulent heat fluxes," *Hydrol. Earth Syst. Sci.* **6**(1), 85–100 (2002).
32. Z. Su et al., "Estimating areal evaporation from remote sensing," in *Proc. of IEEE Int. Geoscience and Remote Sensing Symp (IGARSS 2003)*, (IEEE Cat. No. 03CH37477), Vol 2, no 1, pp. 1166–1168 (2003).
33. F. Li and T. J. Lyons, "Remote estimation of regional evapotranspiration," *Environ. Model. Softw.* **17**(1), 61–75 (2002).
34. E. Webster, D. Ramp, and R. T. Kingsford, "Incorporating an iterative energy restraint for the Surface Energy Balance System (SEBS)," *Remote Sens. Environ.* **198**, 267–285 (2017).
35. W. P. Kustas, "Estimates of evapotranspiration with a one- and two-layer model of heat transfer over partial canopy cover," *J. Appl. Meteorol.* **29**(8), 704–715 (1990).
36. W. J. Shuttleworth and J. S. Wallace, "Evaporation from sparse crops-an energy combination theory," *Q. J. R. Meteorol. Soc.* **111**(465), 839–855 (1985).
37. J. M. Norman, W. P. Kustas, and K. S. Humes, "Source approach for estimating soil and vegetation energy fluxes in observations of directional radiometric surface temperature," *Agric. For. Meteorol.* **77**(3–4), 263–293 (1995).
38. W. Zheng, *Inversion of Evapotranspiration on Urban Land Surface Based on Remote Sensing Data*, Central South University, Changsha, China (2012).
39. Y. Zhang et al., "A modified multi-source parallel model for estimating urban surface evapotranspiration based on ASTER thermal infrared data," *Remote Sens.* **9**(10), 1029 (2017).
40. "NASA Jet Propulsion Laboratory," https://asterweb.jpl.nasa.gov/swir-alert.asp (15 February 2017).
41. K. Zhang, J. S. Kimball, and S. W. Running, "A review of remote sensing based actual evapotranspiration estimation," *Wiley Interdiscip. Rev. Water* **3**(6), 834–853 (2016).
42. Q. Mu, M. Zhao, and S. W. Running, "Improvements to a MODIS global terrestrial evapotranspiration algorithm," *Remote Sens. Environ.* **115**(8), 1781–1800, (2011).
43. W. Yuan et al., "Global estimates of evapotranspiration and gross primary production based on MODIS and global meteorology data," *Remote Sens. Environ.* **114**(7), 1416–1431 (2010).
44. K. Zhang et al., "Satellite based analysis of northern ET trends and associated changes in the regional water balance from 1983 to 2005," *J. Hydrol.* **379**(1–2), 92–110 (2009).
45. K. Zhang et al., "A continuous satellite-derived global record of land surface evapotranspiration from 1983 to 2006," *Water Resour. Res.* **46**(9) (2010).
46. R. Leuning et al., "A simple surface conductance model to estimate regional evaporation using MODIS leaf area index and the Penman-Monteith equation," *Water Resour. Res.* **44**(10) (2008).
47. S. Naeem et al., "Vegetation role in controlling the ecoenvironmental conditions for sustainable urban environments: a comparison of Beijing and Islamabad," *J. Appl. Remote Sens.* **12**(1), 016013 (2018).
48. Z. Jia et al., "Validation of remotely sensed evapotranspiration over the Hai River Basin, China," *J. Geophys. Res. Atmos.* **117**(13), 1–21 (2012).
49. E. Falge et al., "Gap filling strategies for defensible annual sums of net ecosystem exchange," *Agric. For. Meteorol.* **107**(1), 43–69 (2001).
50. A. A. van de Griend and M. Owe, "Bare soil surface resistance to evaporation by vapor diffusion under semiarid conditions," *Water Resour. Res.* **30**(2), 181–188 (1994).

51. J. S. Wallace and C. J. Holwill, "Soil evaporation from tiger-bush in south-west Niger," *J. Hydrol.* **188**–**189**, 426–442 (1997).

52. G. Sun et al., "Stratified spectral mixture analysis of medium resolution imagery for impervious surface mapping," *Int. J. Appl. Earth Obs. Geoinf.* **60**, 38–48 (2017).

53. M. K. Ridd, "Exploring a V-I-S (vegetation-impervious surface-soil) model for urban eco-system analysis through remote sensing: comparative anatomy for cities," *Int. J. Remote Sens.* **16**(12), 2165–2185 (1995).

54. C. Small, "Estimation of urban vegetation abundance by spectral mixture analysis," *Int. J. Remote Sens.* **22**(7), 1305–1334 (2001).

55. C. Wu and A. T. Murray, "Estimating impervious surface distribution by spectral mixture analysis," *Remote Sens. Environ.* **84**(4), 493–505 (2003).

56. Q. Weng, D. Lu, and J. Schubring, "Estimation of land surface temperature-vegetation abundance relationship for urban heat island studies," *Remote Sens. Environ.* **89**(4), 467–483 (2004).

57. S. Phinn et al., "Monitoring the composition of urban environments based on the vegetation-impervious surface-soil (VIS) model by subpixel analysis techniques," *Int. J. Remote Sens.* **23**(20), 4131–4153 (2002).

58. D. Lu and Q. Weng, "Spectral mixture analysis of the urban landscape in Indianapolis with Landsat ETM+ imagery," *Photogramm. Eng. Remote Sens.* **70**(9), 1053–1062 (2004).

59. C. Wu, "Normalized spectral mixture analysis for monitoring urban composition using ETM+ imagery," *Remote Sens. Environ.* **93**(4), 480–492 (2004).

60. L. Li et al., "Discriminating lava flows of different age within Nyamuragira's volcanic field using spectral mixture analysis," *Int. J. Appl. Earth Obs. Geoinf.* **40**, 1–10 (2015).

61. Z. Qin, A. Karnieli, and P. Berliner, "A mono-window algorithm for retrieving land surface temperature from Landsat TM data and its application to the Israel-Egypt border region," *Int. J. Remote Sens.* **22**(18), 3719–3746 (2001).

62. F. Wang et al., "An improved mono-window algorithm for land surface temperature retrieval from Landsat 8 thermal infrared sensor data," *Remote Sens.* **7**(4), 4268–4289 (2015).

63. "ASTER Spectral Library," https://speclib.jpl.nasa.gov/ (14 March 2017).

64. K. Mao et al., "A practical split-window algorithm for retrieving land-surface temperature from MODIS data," *Int. J. Remote Sens.* **26**(15), 3181–3204 (2005).

65. S. K. Ambast, A. K. Keshari, and A. K. Gosain, "An operational model for estimating regional evapotranspiration through surface energy partitioning (RESEP)," *Int. J. Remote Sens.* **23**(22), 4917–4930 (2002).

66. M. Kanda et al., "Roughness lengths for momentum and heat derived from outdoor urban scale models," *J. Appl. Meteorol. Climatol.* **46**(7), 1067–1079 (2007).

67. W. Brutsaert, "Evaporation into the atmosphere," in *SSRN Electronic Journal*, Springer Netherlands, Dordrecht (1982).

68. W. P. Kustas et al., "Determination of sensible heat flux over sparse canopy using thermal infrared data," *Agric. For. Meteorol.* **44**(3–4), 197–216 (1989).

69. B. J. Choudhury, R. J. Reginato, and S. B. Idso, "An analysis of infrared temperature observations over wheat and calculation of latent heat flux," *Agric. For. Meteorol.* **37**(1), 75–88 (1986).

70. S. Liu et al., "Evaluating parameterizations of aerodynamic resistance to heat transfer using field measurements," *Hydrol. Earth Syst. Sci.* **11**(2), 769–783 (2007).

71. K. Yang et al., "Improvement of surface flux parametrizations with a turbulence-related length," *Q. J. R. Meteorol. Soc.* **128**(584), 2073–2087 (2002).

72. Y. Yang et al., "An enhanced two-source evapotranspiration model for land (ETEML): algorithm and evaluation," *Remote Sens. Environ.* **168**, 54–65 (2015).

73. D. Long and V. P. Singh, "A two-source trapezoid model for evapotranspiration (TTME) from satellite imagery," *Remote Sens. Environ.* **121**, 370–388 (2012).

74. D. Long and V. P. Singh, "Integration of the GG model with SEBAL to produce time series of evapotranspiration of high spatial resolution at watershed scales," *J. Geophys. Res. Atmos.* **115**(21) (2010).

75. J. W. Spencer, "Fourier series representation of the position of the Sun," *Search* **2**, 162–172 (1971).

76. S. Liang, "Narrowband to broadband conversions of land surface albedo I Algorithms," *Remote Sens. Environ.* **76**(2), 213–238 (2001).

77. M. A. Friedl, "Relationships among remotely sensed data, surface energy balance, and area-averaged fluxes over partially vegetated land surfaces," *J. Appl. Meteorol.* **35**(11), 2091–2103 (1996).

78. N. A. Brunsell, J. M. Ham, and K. A. Arnold, "Validating remotely sensed land surface fluxes in heterogeneous terrain with large aperture scintillometry," *Int. J. Remote Sens.* **32**(21), 6295–6314 (2011).

79. R. Kormann and F. X. Meixner, "An analytical footprint model for non-neutral stratification," *Boundary-Layer Meteorol.* **99**(2), 207–224 (2001).

80. J. Kleissl, S.-H. Hong, and J. M. H. Hendrickx, "New Mexico scintillometer network: supporting remote sensing and hydrologic and meteorological models," *Bull. Am. Meteorol. Soc.* **90**(2), 207–218 (2009).

81. J. Chávez et al., "Comparing aircraft-based remotely sensed energy balance fluxes with Eddy covariance tower data using heat flux source area functions," *J. Hydrometeorol.* **6**(6), 923–940 (2005).

82. S. Liu et al., "Estimation of regional evapotranspiration by TM/ETM+ data over heterogeneous surfaces," *Photogramm. Eng. Remote Sens.* **73**(10), 1169–1178 (2007).

83. W. W. Verstraeten, F. Veroustraete, and J. Feyen, "Assessment of evapotranspiration and soil moisture content across different scales of observation," *Sensors* **8**(1), 70–117 (2008).

84. E. P. Glenn et al., "Integrating remote sensing and ground methods to estimate evapotranspiration," *Crit. Rev. Plant Sci.* **26**(3), 139–168 (2007).

85. D. Courault, B. Seguin, and A. Olioso, "Review on estimation of evapotranspiration from remote sensing data: From empirical to numerical modeling approaches," *Irrig. Drain. Syst.* **19**(3/4), 223–249 (2005).

86. J. D. Kalma, T. R. McVicar, and M. F. McCabe, "Estimating land surface evaporation: A review of methods using remotely sensed surface temperature data," *Surv. Geophys.* **29**(4–5), 421–469 (2008).

87. H. Su et al., "Modeling evapotranspiration during SMACEX: comparing two approaches for local-and regional-scale prediction," *J. Hydrometeorol.* **6**(6), 910–922 (2005).

88. M. F. McCabe and E. F. Wood, "Scale influences on the remote estimation of evapotranspiration using multiple satellite sensors," *Remote Sens. Environ.* **105**(4), 271–285 (2006).

89. W. P. Kustas and J. M. Norman, "Evaluation of soil and vegetation heat flux predictions using a simple two-source model with radiometric temperatures for partial canopy cover," *Agric. For. Meteorol.* **94**(1), 13–29 (1999).

90. J. M. Norman et al., "Surface flux estimation using radiometric temperature: a dual temperature-difference method to minimize measurement errors," *Water Resour. Res.* **36**(8), 2263–2274 (2000).

91. F. Li et al., "Comparing the utility of microwave and thermal remote-sensing constraints in two-source energy balance modeling over an agricultural landscape," *Remote Sens. Environ.* **101**(3), 315–328 (2006).

92. R. R. Gillies, W. P. Kustas, and K. S. Humes, "A verification of the 'triangle' method for obtaining surface soil water content and energy fluxes from remote measurements of the Normalized Difference Vegetation Index (NDVI) and surface radiant temperatures," *Int. J. Remote Sens.* **18**(15), 3145–3166 (1997).

93. L. Jiang and S. Islam, "Estimation of surface evaporation map over Southern Great Plains using remote sensing data," *Water Resour. Res.* **37**(2), 329 (2001).

94. L. Jiang and S. Islam, "An intercomparison of regional latent heat flux estimation using remote sensing data," *Int. J. Remote Sens.* **24**(11), 2221–2236 (2003).

95. M. C. Anderson et al., "A climatological study of evapotranspiration and moisture stress across the continental United States based on thermal remote sensing: 1. Model formulation," *J. Geophys. Res. Atmos.* **112**(10), 1–17 (2007).

96. A. N. French et al., "Surface energy fluxes with the Advanced Spaceborne Thermal Emission and Reflection Radiometer (ASTER) at the Iowa 2002 SMACEX site (USA)," *Remote Sens. Environ.* **99**(1–2), 55–65 (2005).

97. W. W. Verstraeten, F. Veroustraete, and J. Feyen, "Estimating evapotranspiration of European forests from NOAA-imagery at satellite overpass time: towards an operational processing chain for integrated optical and thermal sensor data products," *Remote Sens. Environ.* **96**(2), 256–276 (2005).

98. K. Wang et al., "A simple method to estimate actual evapotranspiration from a combination of net radiation, vegetation index, and temperature," *J. Geophys. Res. Atmos.* **112**(15) (2007).

99. S. W. Running et al., "A continuous satellite-derived measure of global terrestrial primary production," *Bioscience* **54**(6), 547–560 (2004).

100. L. T. Wong and W. K. Chow, "Solar radiation model," *Appl. Energy* **69**, 191–224 (2001).

101. R. G. Allen et al., "Satellite-based energy balance for Mapping Evapotranspiration with Internalized Calibration (METRIC)—applications," *J. Irrig. Drain. Eng.* **133**(4), 395–406 (2007).

Yu Zhang is a PhD candidate at China University of Mining and Technology. He is engaged in the study of urban heat flux and urban climate.

Long Li is a lecturer at China University of Mining and Technology. His study field is remote sensing monitoring of environment and disasters.

Kai Qin is an associate professor at China University of Mining and Technology. His study field is remote sensing monitoring of environment and disasters.

Yuchen Wang is a PhD candidate at China University of Mining and Technology. He is engaged in the study of urban heat flux and urban climate.

Longqian Chen is the professor of the Department of Land Resource Management, at China University of Mining and Technology. His major research directions focus on geoscience and environmental science, and in particular on the urban heat environment.

Xiaoyan Yang is a PhD candidate at China University of Mining and Technology. He is engaged in the study of urban heat flux and urban climate.